

Chapter 1

Introduction

1.1 Materials

Rubbers are chemically crosslinked linear polymers. Their most notable characteristic is their mechanical behavior, i.e. they can withstand large strains and can be loaded multiple times while recovering their initial shape—apart from a small permanent set—upon unloading. Due to the permanent nature of the chemical bonds between the polymer chains, rubbers distinguish themselves from thermoplastic polymers in that they cannot be melted, which implies different processing routes.¹ Compared to thermoset resins, rubbers feature a lower crosslinking density and a higher molecular weight, providing for the lower modulus and higher strain at break.

Historically, the first type of rubber known to mankind was natural rubber. More than 3,000 years ago, native tribes in Central America used rubber balls obtained from the latex of the hevea plant for their now-famous ball games [1]. The next big step in the history of rubber is due to Charles Goodyear, who discovered the process of sulfur vulcanization in 1839. This made rubber products suitable for a wide variety of applications, which were previously excluded from the use of unvulcanized rubber due to the poor mechanical performance and stability. The first synthetic rubbers were developed in the 1930s and became available on an industrial scale in the 1940s, when the supply of natural rubber was limited due to the Second World War. Nowadays, numerous types of rubbers are available on the market, each serving certain purposes. Rubbers are widely used in applications such as tires, dampers, tubes, seals, belts, cable coatings, footwear, textiles, and others.

¹ Sometimes thermoplastic elastomers are also classified as rubbers. These materials are melt-processable and are physically crosslinked rather than chemically.

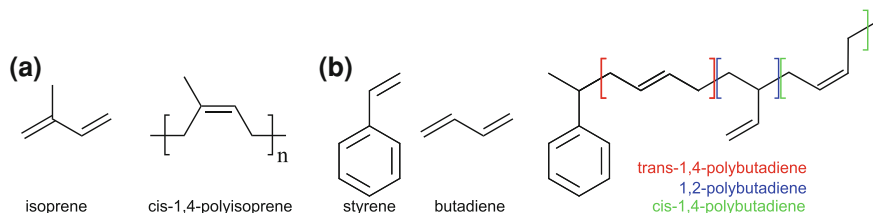


Fig. 1.1 Chemical structures of **a** isoprene and cis-1,4-polyisoprene; **b** styrene, butadiene and its types of appearance in SBR

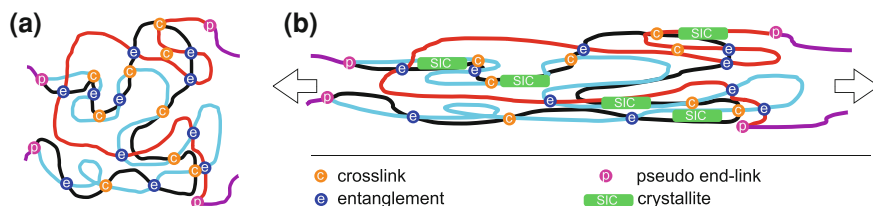


Fig. 1.2 Sketch of network structure of natural rubber: **a** undeformed, **b** stretched beyond SIC onset (Adapted with permission from Ref. [4], copyright 2013 American Chemical Society)

1.1.1 Rubber Types

Natural rubber is obtained from the latex of the rubber tree *Hevea brasiliensis*.² After the latex has been harvested from the bark of the tree, it is purified and pressed. The drying process takes place either in air or in smoke. The smoking process conserves the rubber and serves as a protection against fungi. While the smoked version is more relevant on an industrial scale, the air dried version is preferred in science due to its purity (e.g. pale crepe grade, Fig. A.6).

Chemically, natural rubber consists mainly of cis-1,4-polyisoprene (Fig. 1.1a). The perfect stereoregularity (100 % cis) renders NR crystallizable, either by cooling in the quiescent state or by stretching. Besides the polyisoprene, NR contains around 6 % impurities, among which the biggest percentage share the lipids, proteins and other low molecular weight carbohydrates [2]. The polyisoprene chains in NR are linear, but end-functionalized, producing a three-dimensional network with proteins and lipids acting as crosslinkers (Fig. 1.2) [3, 4]. This network gives the comparatively high strength to the unvulcanized rubber, the so called green strength.

In contrast to NR, synthetic isoprene rubber (IR) is not perfectly stereoregular, having a trans content of at least 1.5 % [5, 6]. The irregularity impedes crystallization, shifting the onset strain of SIC to larger strains as compared to NR [7–9]. This is reflected in inferior tensile properties and a reduced tear resistance [10]. Due to the absence of a network in the unvulcanized (green) IR, the green strength is lower by a

² Other sources, like dandelion and guayule (*Parthenium argentatum*), have been explored, but are not significant in practice.

factor of 60 [5]. IR is mainly used as a processing aid to facilitate mixing of NR [6]. The yearly consumption of IR is around 20 times less compared to NR [11].

The third type of rubber studied in this work is styrene-butadiene rubber (SBR). Chemically, it is a statistical copolymer of styrene (commonly around 25 %) and butadiene (around 75 %) (Fig. 1.1b). The polymerization is carried out either anionically in solution or radically in emulsion. The first gives solution SBR (S-SBR), the latter emulsion SBR (E-SBR). The type of polymerization determines the vinyl content,³ which is higher in S-SBR. SBR has almost the same tensile strength as NR, and this at much lower cost. Therefore, it has replaced NR in some applications, notably in passenger car tires. Both S-SBR and E-SBR are used in tires. However, the tear resistance of SBR is inferior to NR, since SBR does not strain-crystallize.

Other rubber types include, amongst others, polybutadiene, polychloroprene, ethylene-propylene rubber and butyl rubber. They find use due to specific properties regarding mechanical hysteresis, gas permeability, chemical stability, oil resistance, heat resistance, ozone aging, flame retardance, glass transition temperature or adhesion [6].

1.1.2 Vulcanization

In the vulcanization process, the chemical crosslinking reaction takes place and the rubber part obtains its final shape. Two types of crosslinking systems are relevant, and both have been used in this work:

- sulfur vulcanization
- peroxide vulcanization.

Industrially, the sulfur vulcanization is more widely used. Sulfur is added in elemental form during the mixing process. Upon curing, it attacks the unsaturated bonds in the backbone or at side groups of the polymer chain and forms sulfide bridges. Depending on the vulcanization system, various types of sulfide bridges with different lengths can be formed. Without the proper use of additives, this crosslinking reaction would take several hours [12].⁴ Zinc oxide and stearic acid are usually added as activators, and organic compounds, bearing a $N=C-S_2$ functionality, serve as accelerators [13]. The precise role of these chemicals in the crosslinking mechanism is still subject to research [14]. The common understanding is that stearic acid aids in the solubilization of the zinc oxide, which then forms a complex with the accelerators and activates the sulfur [15].

Industrial rubber recipes often contain several accelerators or boosters. Retarders are added to extend the scorch time to avoid premature curing during processing.

³ Vinyl groups result from the 1,2-polymerization of butadiene, in contrast to the more common 1,4-polymerization.

⁴ Own tests showed that a standard formulation of natural rubber, including 1 phr sulfur, 1 phr stearic acid and 1.5 phr CBS (accelerator, N-cyclohexyl-2-benzothiazole-sulfenamide), but not containing any zinc oxide, would not vulcanize within 1 h at 160 °C.

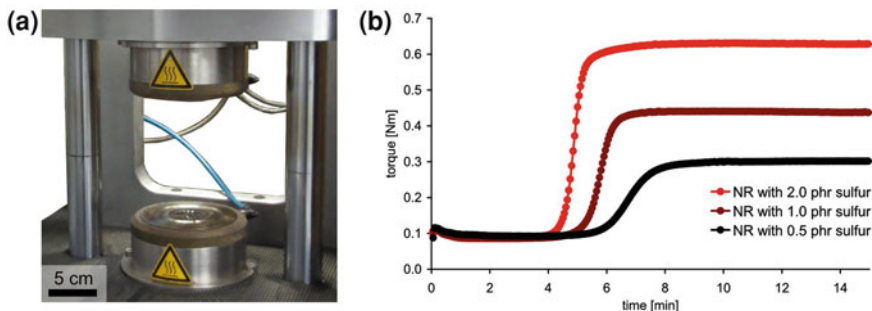


Fig. 1.3 **a** Photograph of the vulcameter dies, between which the sample is placed for analysis. **b** Vulcameter curves (torque over time) at 160 °C from NR compounds with various crosslinking densities (based on #2 (see list of materials in Sect. A.6), keeping the sulfur-CBS ratio constant)

Peroxide vulcanization, on the other hand, is mainly used in a scientific context in model compounds. The chemistry is simpler and no addition of particulate additives like zinc oxide is required. The peroxide decomposes into two radicals at the vulcanization temperature and abstracts a hydrogen from a saturated carbon-carbon bond. The resulting polymer radicals combine to form a direct crosslink without a bridge inbetween [12].

The crosslinking reaction is usually carried out at temperatures between 120 and 180 °C. Following the Arrhenius equation, the curing process is accelerated by increasing the temperature, but care must be taken to avoid thermal degradation. The vulcanization time is measured by a vulcameter, also called rubber process analyzer (Fig. 1.3a). A green rubber sample is placed between two dies, which have been heated to the vulcanization temperature. The dies are firmly pressed together to avoid wall slip and one of the dies starts a sinusoidal rotating motion, subjecting the rubber sample to a shear stress. The torque required to apply a certain shear strain amplitude is taken to be proportional to the crosslinking density, following the simple relation $G = NkT^5$ [16]. After some time, the vulcanization process is complete and the torque reaches a plateau. The time it takes to reach 90 % of the plateau level is commonly referred to as t_{90} and taken as vulcanization time. Depending on the geometry of the mold and the thickness of the rubber part, some additional time might be added to this value.

1.1.3 Fillers

In order to meet the requirements imposed by numerous applications, almost all rubber parts consist of filled rubbers, i.e. they are a composite of the vulcanized

⁵ G is the shear modulus; N is the number of chains per unit volume; k is the Boltzmann constant; T is the absolute temperature.

Table 1.1 Typical tire tread compounds for passenger car and truck tires. Additives are not listed. The values are given in phr. Adapted from [17]

	Passenger car tire tread	Truck tire tread
E-SBR	65	
BR	35	
NR		100
Carbon black	70	50
Processing oil	40	10

rubber matrix and a filler. The reason for the addition of a filler can be twofold: either a reduction of the product cost, or an improvement in the (mechanical) properties. The first group is called non-reinforcing fillers, or extenders (e.g. calcium carbonate and other micron-size particulate fillers), the latter reinforcing fillers [12]. The most important reinforcing fillers are carbon black and precipitated silica. They enhance the modulus, increase the tensile strength by a factor of up to 10, and also benefit the abrasion, tear and damping behavior [6].

In rubber technology, the filler content is specified in parts per hundred rubber (phr) by weight, i.e. the rubber matrix constitutes 100phr by definition. In a blend of different elastomers, the sum of all elastomer matrix components adds up to 100phr [17]. Typical recipes for passenger car and truck tire treads are listed in Table 1.1. The carbon black loading is between 40 and 90phr. In passenger car tires, SBR is preferred over NR due to its lower price. In truck tires, however, due to the high loads acting on the tire and due to the requirement for increased mileage, NR is preferred over SBR, e.g. to avoid failure by so-called chipping and chunking.

Over the last two decades, carbon black has increasingly been replaced by silica in passenger car tires, especially winter tires. In truck tires, hybrid filler systems, featuring silica and carbon black, have been introduced.

Processing oil is added to facilitate the processing by lowering the viscosity. It also serves to adjust the hardness and to compensate for high carbon black loadings.

Carbon blacks for reinforcing purposes are produced in the so-called furnace process: Aromatic oil is injected into a fast stream of hot (1200–1900 °C) combustion gases (from the combustion of other carbohydrates), and subsequently quenched with water. Afterwards it is filtered, pelletized and dried. Between the injection and the quenching a partial oxidation takes place due to the controlled presence of oxygen, which is adjusted to substoichiometric concentrations [18]. Within milliseconds, the primary particles are formed from nuclei of solid reaction products, which then fuse together to form aggregates. Besides growth by collision of primary particles, also a gradual deposition of other carbonaceous reaction products on the surface of primary particles and aggregates takes place, acting like a glue between the primary particles and increasing the stability and compactness of the aggregates [19, 20]. Aggregates typically consist of 8–60 primary particles [21–25]. These aggregates cannot be broken up in subsequent processing steps (e.g. rubber compounding). Adjustments in the reaction temperature, reaction time and flow turbulence determine the particle size and aggregate structure [18].

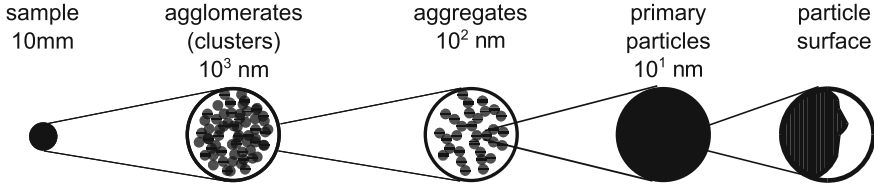


Fig. 1.4 Schematic representation of the hierarchical structure in a carbon black filled rubber (Adapted from Schneider [27])

Carbon black is available in numerous grades for specific purposes, classified by surface area and structure. The standard classification follows the *Nabc* nomenclature according to ASTM D-24 [17]. *N* stands for *N*ormal curing.⁶ The first digit, *a*, refers to the diameter of the primary particles, which is, as a rule of thumb, $10a$, measured in nm, i.e. an N300 grade has a primary particle diameter around 30 nm. The other two digits, *b* and *c*, are assigned based on the structure and surface area. The packing density and the degree of branching within an aggregate determine its structure, which is characterized by dibutylphthalate absorption,⁷ while the surface area is analyzed by nitrogen, iodine or CTAB⁸ adsorption [17, 18]. Depending on the size of the probing substance, it penetrates into pores and other smaller entities, thus lending the method a sensitivity in a certain size range [26].

The architecture of carbon black is schematically shown in Fig. 1.4. Typically during the processing of the rubber composite, aggregates cluster together to form agglomerates, which are more loosely bound. On an even larger length scale, provided the filler content is sufficiently high, a network superstructure can be established.

The description of the complex carbon black structure in mathematical terms is rather daunting. The most widely used concept is the fractal theory. The foundations for this theory were laid by Benoit Mandelbrot in 1975, describing self-similar geometries. A geometry is self-similar, when each part of it is constituted by a geometric reduction of the whole [28, 29]. This implies scaling laws for geometric properties like the volume (mass) and surface area. Following fractal theory, the area of a rough surface depends on the length r of the yardstick that one uses to measure the area S :

$$S(r) = r^{2-D_s}. \quad (1.1)$$

A smooth surface has a fractal dimension D_s of 2, whereas for an infinitely rough surface $D_s = 3$.

Applying the fractal concept to three dimensions, the relation for mass fractals reads:

$$M(r) = r^{D_m}. \quad (1.2)$$

⁶ Nowadays, all industrially relevant standard carbon blacks for mechanical reinforcement are of *N* type, but historically other grades were common.

⁷ OAN: oil absorption number.

⁸ Cetyltrimethyl ammonium bromide.

Accordingly, a space-filling solid body has a mass fractal dimension D_m of 3, and with increasing pore volume the mass fractal dimension decreases.

Theoretically, the self-similarity and thus the scaling laws 1.1 and 1.2 extend over all size ranges. In practice, there are upper and lower limits. For instance, in the case of fractal aggregates, the scaling holds only for $r_0 < r < R$, where r_0 is the size of a primary particle and R is the size of the aggregate. The fractal dimension of aggregates can actually be predicted by theories. Depending on the growth mechanism, whether it is diffusion-limited or reaction-limited, whether growth takes place by the addition of primary particles to the aggregates or by the clustering of existing aggregates, different fractal dimensions D_m are obtained. They range from 1.75 to 2.2 [29]. As pointed out above, the reality is not as simple as the theory. Due to the inhomogeneity of the reaction conditions along the gas jet in a furnace reactor, several growth mechanisms might occur. The addition of carbonaceous material even smaller than the primary particles adds to the complexity of the growth mechanism. This is further exacerbated by the polydispersity. While the polydispersity of the primary particles is quite low, the aggregate sizes cover a rather broad range, obscuring a clear cutoff size of the scaling region. Not only are the aggregates polydisperse, they have also been observed to be constituted of a rather small number of primary particles. This restricts the scaling law to a rather small region, which rarely covers even a single decade.

In fact, even though fractal theory is the most widely used approach for the description of carbon black geometries, it is not undisputed in the research community. The popularity of the fractal concept in the field of carbon black rather seems to stem from the simplicity of the fractal concept and from the lack of alternative theories rather than from its ability to precisely account for the experimental observations. This conflict is nicely expressed by Huber and Vilgis, who in one of their papers, dealing with carbon black aggregates, use the fractal theory “[...] only to describe the structure, rather than to suggest that the structure *is* fractal” [30].

The beauty of the fractal concept is that it is easily applicable to scattering data, which is one of the favorite methods to characterize carbon blacks. Due to the sizes involved, scattering takes place in the SAXS and USAXS regimes. Bale and Schmidt derived a power law relation between the scattering intensity I and the scattering vector q (Sect. 1.2.2) [31, 32]. For mass fractals, the fractal dimension D_m can be obtained directly from the negative slope of a double logarithmic scattering plot, which is obtained from a slice of a two-dimensional isotropic scattering pattern:

$$I(q) = q^{-D_m}. \quad (1.3)$$

Equation 1.3 holds in the region $1/R \ll q \ll 1/r_0$. For surface fractals, the following relation holds in the region $q \gg 1/r_0$:

$$I(q) = q^{6-D_s}. \quad (1.4)$$

In the field of scattering, the polydispersity problem is aggravated by the fact that the small angle scattering intensity does not represent the number average of

scatterers, but rather the seventh moment of the number density distribution, i.e. larger scatterers contribute very significantly [33]. Martin showed that if the polydispersity follows a power law distribution, which is a well-founded assumption, the dependence of the scattering intensity of the surface fractal dimension vanishes [34]. This was later confirmed by Beaucage and Hjelm [35, 36]. Both argue that the surface fractal regime is only apparent, but in reality is caused by polydispersity. Ruland backs up this claim, listing numerous published electron microscopy studies, proving that the surface of carbon black is smooth [37], while Beaucage points out that different electron microscopic methods yield different surface roughnesses [26]. Heinrich and Klüppel developed a model to describe the structure of carbon black based on its formation [38].

Beaucage developed a unified model, incorporating several scattering regimes into one equation. The contributions from the Guinier regimes and fractal regimes (Sect. 1.2.3) are weighted by physically motivated scalars and are superimposed using a set of empirical error functions, which secure that each scattering term only contributes to the corresponding regime [39]. While the unified model removes some of the ambiguity in the rather arbitrary individual fitting of the power law regions and crossovers, it provides only limited novel physical insights due to the partially empirical nature of the equation.

It should be mentioned, however, that independent methods also suggest a fractal structure. Klüppel demonstrated that the number of adsorbed gas molecules on a carbon black surface relates to the adsorption cross section of the molecule following a power law scaling [40]. Assuming a monolayer adsorption mechanism, this suggests a fractally rough surface in the probed size range. Schröder showed that the adsorption not only depends on the surface topography, but also on the distribution of adsorption sites of various energy levels [41].

A dependence between aggregate mass fractal dimension and filler loading is to be expected due to the presence of agglomerates [42], introducing crossterms in the scattering relation. This has indeed been observed [43]. On the contrary, a change in surface fractal dimension with filler loading, as observed by Fröhlich et al. [44], is beyond what is expected by theory. Also the broad ranges of values and the lack of agreement between different publications confirm the impression that current theory is insufficient to precisely describe the reality. Some of the experimentally obtained fractal dimensions even lie out of the physically possible range, e.g. mass fractal dimension less than unity are not physically sound [43].

For instance, the mass fractal dimensions D_m of N330 obtained through SAXS by different groups vary over a broad range between less than unity and 2.0 [43, 44]. TEM (transmission electron microscopy) measurements of the same carbon black grade yield $D_m = 2.4$ [45]. Theoretically, assuming a cluster-cluster aggregation process for the formation of aggregates in the furnace reactor, carbon black aggregates should have a mass fractal dimension D_m of 1.78 [40, 46].

The situation is further complicated by the fact that the classical fractal concept solely describes isotropic structures. Despite the presence of anisometric carbon black aggregates (e.g. ellipsoidal or linear [45, 47]), the isotropy of the scattering patterns seems to suggest the applicability of fractal theory. However, the isotropy

only stems from the non-preferential orientational distribution of anisometric objects. Therefore, the application of isometric concepts on length scales of the aggregates can only serve as a rather coarse and simplified characterization of the real structure. This limitation becomes obvious when the black-filled rubber is deformed. Anisometric objects orient along the principal strain axis, and thus the scattering patterns become anisotropic. The classical fractal theory is not applicable under these conditions. Instead of using self-similar concepts, self-affinity can now be postulated, i.e. *each part is a linear geometric reduction of the whole but with ratios depending on direction* [29]. In other words, a self-affine fractal becomes self-similar, when it is scaled with a constant along at least one of the dimensions. This defines a self-affine mass fractal as follows:

$$M(ax_1, ax_2, a^H x_3) = a^{D_m} M(x_1, x_2, x_3), \quad (1.5)$$

where M is the mass, x_i are the spatial dimensions, a is an arbitrary scalar, and H is the Hurst exponent [27]. Other definitions exist. Self-similarity is a special case of self-affinity ($H = 1$). Several authors pointed out that, due to the introduction of the Hurst exponent H , the fractal dimension of a self-affine fractal is not uniquely defined. In fact, very different self-affine structures can have the same fractal dimension [48, 49].

1.1.4 Reinforcement Mechanisms

In general terms, *reinforcement* is the improvement of material properties. More specifically, rubber materials can be reinforced in order to exhibit an increased stiffness, modulus, rupture energy, tear strength, tensile strength, fatigue resistance and/or abrasion resistance [50]. The reinforcing mechanism in filled rubbers is still not fully understood [19, 51, 52], but numerous literature is available pointing at the contributions of several factors.

Examples for the enhanced tensile properties by filler reinforcement are shown in Fig. 1.5. Payne showed, that the small-strain storage modulus of butyl rubbers can be enhanced by as much as 200 times by the addition of carbon black [53, 54].

The filler effect is less pronounced in strain-crystallizing rubbers, such as natural rubber, due to the inherent self-reinforcement (Fig. 1.5b).

In the following, the three main factors of filler reinforcement are briefly summarized.

1.1.4.1 Hydrodynamic Strain Amplification

The basic concept of strain amplification is that due to the rigidity of the filler phase (in contrast to the soft rubber matrix), the rubber matrix undergoes larger deformations than the external deformation would suggest. Gehman expressed this nicely: “[In

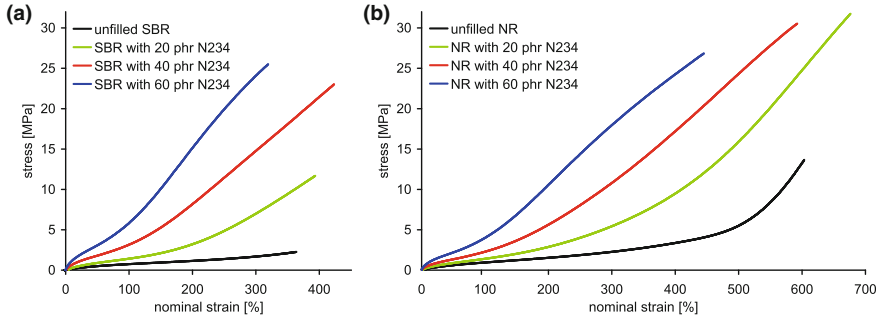


Fig. 1.5 Stress-strain curves for **a** SBR [#40, #41, #42, #43] and **b** NR [#2, #3, #4, #5] compounds with various filler loadings. The reinforcing effect is clearly visible (For sample nomenclature, see Sect. A.6)

filled rubbers,] rubber works at a higher point on its stress-strain curve” [55]. In the context of a viscous particle suspension, the physics behind this effect have been worked out by Einstein more than 100 years ago. He proposed an equation relating the viscosity of the suspension η to the amount of filler volume content ϕ [56]. For spherical particles, the equation reads

$$\eta = \eta_0 (1 + 2.5\phi), \quad (1.6)$$

where η_0 is the viscosity of the unfilled fluid. Equation 1.6 is only valid for non-interacting spheres, i.e. the filler content must be sufficiently low. Einstein’s relation was applied to the modulus E of filled rubbers by Guth and Gold and extended for a correctional quadratic term, taking care of the filler interaction in concentrated systems:

$$E = E_0 (1 + 2.5\phi + 14.1\phi^2). \quad (1.7)$$

The quadratic term is empirical and other factors have frequently been suggested [52, 56]. The equations for hydrodynamic strain amplification can only serve as a rough approximation of the reinforcement due to neglecting effects like strain rate and strain history [57].

Medalia quantitatively introduced the concept of an effective filler volume [55, 58]. The effective filler volume includes not only the filler itself, but also the passive rubber fraction, i.e. the part of the rubber that is occluded in the aggregate pores and is trapped in the agglomerate structure and thus does not undergo the same deformation as the rubber chains in the bulk phase of the composite. The effective filler volume depends on the structure of the carbon black and its dispersion [20, 26, 40, 59]. Typical values for the ratio of the effective filler volume to the nominal filler volume range from 1.3 to 2.0.

As mentioned above, the strain amplification was originally applied to the modulus of the material, i.e. to the small strain region, which can be approximated by linear

elasticity. It is also applicable to the strain in general. According to Bueche and Smallwood, the strain is amplified by a factor of $\frac{1}{1-\phi^n}$, where the exponent n depends on the geometry of the filler particles [56, 60, 61].

Even though the concept of strain amplification is widely accepted, the direct proof by experimental measurement of the matrix strain is difficult. Approaches include mechanical tests [62, 63], NMR (nuclear magnetic resonance spectroscopy) [60, 64], SANS (small angle neutron scattering) [59, 65–67] and WAXD [68, 69]. The underlying assumption is that a unique relation between the measured quantity ψ (e.g. stress, crystallinity, orientation) and strain ϵ exists, which applies to the unfilled material as well as to the matrix of the filled material [63, 68]:

$$A_{\psi, \text{filled}}(\epsilon) = \frac{\epsilon_{\text{unfilled}}}{\epsilon_{\text{filled}}} \bigg|_{\psi} = \frac{\epsilon_{\text{matrix}}}{\epsilon_{\text{filled}}} \bigg|_{\psi}, \quad (1.8)$$

where $A_{\psi, \text{filled}}$ is the strain amplification factor of the filled material for the quantity ψ . For instance, let the strain in a filled rubber be half of the strain in an unfilled reference at the same stress, then the mechanical strain amplification factor is two. The concept of the mechanical strain amplification has proven to be useful as long as the reinforcing capability of the filler is high, such as in carbon black filled systems [63], and the strain is larger than the Payne regime, i.e., above 20 %, but below the SIC onset [64]. Given that hydrodynamic effects are not the only source of reinforcement, and also numerous other mechanisms like filler–filler networks and adsorption of polymer at the filler surface (immobilized layer of bound rubber, filler particles as additional network crosslinks) have to be considered, quantitative deviations from a constant strain amplification are to be expected and have indeed been observed [60, 64].

In general, the strain amplification factors obtained by different methods do not agree, because the methods are sensitive to different characteristics. Furthermore, it is often overlooked that the concept of strain amplification is not applicable at high carbon black loadings, since above the overlap concentration of the agglomerates, other reinforcing mechanisms set in (Sect. 1.1.4.2) [20]. Some SANS studies did not find any overstrain in the matrix [66, 67].

1.1.4.2 Filler–Filler Interaction

At filler loadings below the overlap concentration, no filler network exists and the load transfer takes place through the rubber matrix, implying the strain amplification as pointed out in the previous section. On the contrary, above the overlap concentration, a filler network is established, and the stresses are transferred directly via the agglomerates. Since the modulus of this network is much larger than that of the rubber, the filler network is the dominating element in this regime [20]. The existence of the filler network is the reason why aggregated structures have better reinforcing properties than completely dispersed fillers [70].

1.1.4.3 Filler Surface and Interphase

The processes at the interface between the rubber chains and the carbon black filler surface is still subject to current research, even though the notion seems to prevail that the interaction is mainly physical in nature, i.e. physisorption and Van-der-Waals interaction dominate over chemical bonding [51, 71]. Applying the macroscopic concept of surface tension and internal pressure to the particle interface, adhesive failure at the filler surface is hindered by these factors alone as long as the particles are sufficiently small, i.e. below 50 nm [51]. Indeed, it is observed that the reinforcing effect increases with decreasing particle size, and that above a certain particle size the reinforcing effect vanishes. The minor role of chemical interaction was confirmed by placing different amounts of reactive groups along the polymer chains. Despite the presence of more reactive groups, the polymer-filler interaction was not enhanced [51]. The idea of physical interaction implies that chains are able to slide along the filler surface, causing hysteresis [51].

Due to the physical adsorption of the polymer chains on the carbon black surface, their mobility is restricted, resulting in an immobile layer, also called glassy layer. The presence of this layer is suggested by DEA (dielectric analysis) [40, 72], DMA (dynamic mechanical analysis) [50], NMR [73], chemical extraction [74] and 3D TEM [75, 76], even though direct evidence is still lacking [67, 71]. The restriction of the polymer mobility on the filler surface is seen in analogy to thin films deposited on substrates, where an increase in the glass transition temperature T_g of the order of 100 K is observed [54]. A more detailed model describes the immobile layer in terms of a gradual transition from a highly immobilized state directly at the surface to bulk-like mobility further away from the surface [77]. The thickness of this transition region is said to range between 1 and 10 nm.

The role of the interphase becomes increasingly important as the particle size is reduced and the specific surface is increased. It further contributes to the superior reinforcing ability of smaller particles. While semi-reinforcing carbon blacks have a specific surface of less than 45 m²/g, reinforcing fillers have around 65–140 m²/g [17].

1.1.4.4 Self-Reinforcement by Strain-Induced Crystallization

A matrix-inherent reinforcement mechanism is the strain-induced crystallization [78]. Strain-crystallizing elastomers partly crystallize if the exerted strain exceeds a certain threshold. This process is governed by the reduction of enthalpy, which depends on the molecular architecture of the polymer chain. A critical prerequisite for the ability to crystallize is the absence of large sidegroups. A high stereoregularity (cis/trans) is required if the backbone contains double bonds (cf. tacticity effects in vinyl thermoplastics). Natural rubber is the most prominent elastomer that exhibits SIC. Other

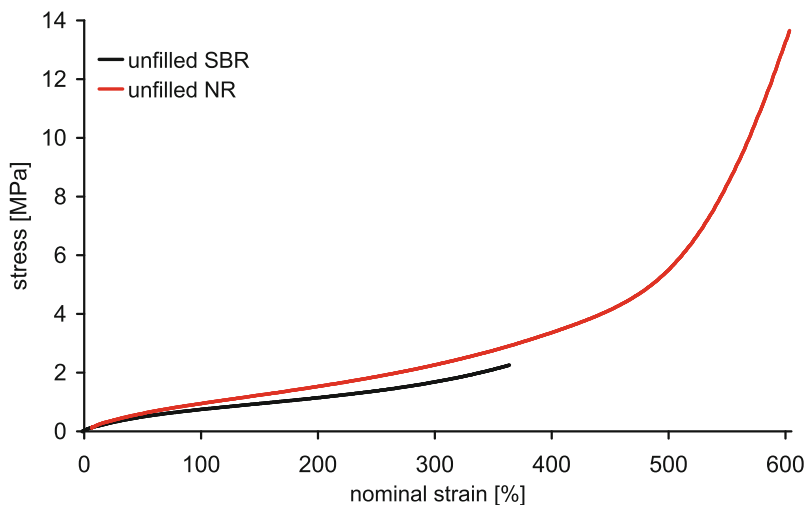


Fig. 1.6 Stress–strain curves for NR and SBR. The stress upturn of NR can be assigned to the reinforcing effect of strain-induced crystallization. The detailed recipes are listed in Sect. A.6 [#2, #40]

strain-crystallizing elastomers include isoprene rubber (IR) [5, 10],⁹ chloroprene rubber (CR) [78, 80–83], butyl rubber [84] and butadiene rubber [84].

Crystallites can be thought of as additional crosslinking points or as rigid reinforcing particles, strengthening the otherwise amorphous rubber [85, 86]. Thanks to SIC, the strength at break and the crack propagation behavior of NR are superior to those of non-crystallizing synthetic rubbers (Fig. 1.6).¹⁰ The beauty of the self-reinforcement is that the crystallization process occurs only in those regions which are subjected to large strains, while the rest of the product maintains its elastic properties. Upon removal of the load, the crystallization is reversible. The drawback is the complex relationship between SIC and temperature, time and multiaxial strain fields. At elevated temperatures and on very short time scales SIC is reduced. This makes an implementation of SIC into constitutive models difficult [87, 88].

1.1.5 Mechanical Behavior

Since rubber is mainly used as a structural material, its mechanical properties are of utmost importance. While the basic elastic behavior can be traced back to simple

⁹ Only IR grades with high cis-content can undergo SIC. Furthermore, IR crystallizes only in the crosslinked state [79].

¹⁰ Of course, the comparison should not be taken too quantitatively. NR and SBR are chemically different, and moreover NR has an inherent network resulting from its natural impurities and endgroup functionalization. However, from a practical point of view, reinforced SBR can often replace reinforced NR in less demanding applications.

entropy elasticity, the problem becomes somewhat more involved when dealing with filled rubbers or strain-crystallizing rubbers.

1.1.5.1 Origin of Rubber Elasticity

As opposed to metals, the elasticity of rubbers is driven by entropy and not by enthalpy. In a stretched rubber, the chain segments can assume fewer conformations, reducing the entropy, and thus increasing the free energy. In other words, the larger the distance between the chain ends, the fewer paths are available to connect the ends by a given number of segments. The increase in free energy is balanced by the work caused by the external force acting on the rubber. For a single freely jointed chain, following Gaussian chain statistics, the relation between the magnitude of the end-to-end vector R and the force f reads as follows:

$$f = \frac{3kT}{nb^2} R, \quad (1.9)$$

where n is the number of statistical chain segments and b is the chain segment length [89].

Extending the concept from a single chain to N chains per unit volume in three dimensions, the change in the free energy ΔF upon uniaxial elongation is, under the assumption of incompressibility [90]:

$$\Delta F = \frac{NRT}{2} \left(\alpha^2 + \frac{2}{\alpha} - 3 \right). \quad (1.10)$$

Here, α is the stretch ratio.¹¹ At constant temperature, the free energy ΔF equals the work w done on the system. The work is stored as elastic strain energy, following the definition of a hyperelastic material model. Equation 1.10 represents one of the simplest constitutive equations for the mechanics of elastomers. With $NRT = C_1$, C_1 being an empirical constant, it can be identified as the so-called Neo-Hookean law. It is a special case of the more general Mooney-Rivlin constitutive law. Nowadays, numerous constitutive models are available and are an essential basis for any finite element code [91].

The derivative of the strain energy density w with respect to the displacement gives the stress σ :

$$\sigma = NRT \left(\alpha - \frac{1}{\alpha^2} \right). \quad (1.11)$$

¹¹ The stretch ratio α is defined as $\alpha = \frac{l}{l_0}$, where l_0 is the undeformed length and l is the deformed length. The relation between the stretch ratio α and the strain ϵ is $\alpha = 1 + \epsilon$.

1.1.5.2 Mullins Effect

The Mullins effect describes the history dependence of the large strain mechanical behavior of filled and unfilled elastomers [92]. This stress softening effect is more pronounced in filled rubbers. When stretching a rubber for the first time above the previous maximum strain, filler–filler bonds break and rubber chains slide along the filler surface [51]. In the consecutive stretching cycles, the stress at a given strain level below the previous maximum strain will be reduced (Figs. 1.7a and 4.5). In addition to the filler, viscous matrix effects also play a role. The Mullins effect is most pronounced during the first three loading cycles and vanishes after ten cycles. After very long waiting time, preferentially at elevated temperature, the Mullins effect is reversible [51, 93]. The Mullins effect should be taken into account when dealing with the reproducibility of mechanical experiments. In order to exclude undesired effects in the study of bulk materials, multiple cyclic loading to the maximum investigated strain prior to the experiment is advisable (so-called *demullinization*). In contrast to this, in the context of static crack growth and tear fatigue, the material in front of the crack tip usually was not subjected to excessively large strains before being reached by the crack front.

1.1.5.3 Payne Effect

A peculiar effect in filled rubbers in the low strain regime is the Payne effect. It nicely connects the filler structure with the dynamic mechanical behavior. The Payne effect is expressed as a drop in storage modulus G' as a function of strain amplitude in a strain sweep DMA experiment (Fig. 1.7b) [53]. Between 0.1 and 15 % strain, G' drops by roughly a factor of ten. The magnitude of the drop depends on the filler structure and on the temperature. The underlying physical reason is the breakdown of filler–filler interactions [71]. Sotta et al. postulated the breakdown of glassy bridges between agglomerates [54]. The Payne effect is not found in unfilled rubbers, but it occurs in carbon black-filled liquids [40, 94]. The fact that the Payne effect is less pronounced at high temperatures hints at the temperature sensitivity of the filler bridges; thus supporting the idea of overlapping glassy layers serving as bridges to establish a network [26, 50]. In terms of strain amplification, the Payne effect can be interpreted in that upon the destruction of the filler network, previously trapped rubber rejoins the deformed phase and thus the effective filler volume is decreased [26]. After a sufficiently long waiting time, the material can recover from the Payne effect [95]. The Payne effect has been implemented into models [40, 61].

1.1.5.4 Fracture and Tear Fatigue of Elastomers

Besides the small-strain dynamic properties, the tear and rupture properties of rubbers are highly relevant for the material performance in various applications. In some cases, tear fatigue is the lifetime-limiting failure mechanism. The beginnings of

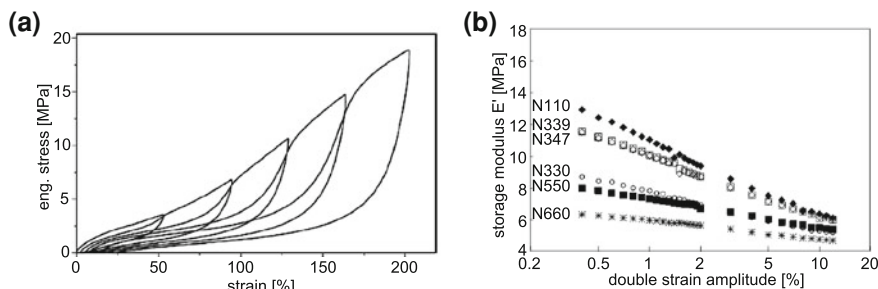


Fig. 1.7 **a** Illustration of the Mullins effect, exemplified on E-SBR with 80phr N339. (Adapted with permission from Ref. [40], copyright 2003 Springer.) **b** Illustration of the Payne effect in filled natural rubbers with 50phr of various filler grades. The more reinforcing the filler, the more pronounced the drop in the storage modulus E' . The experiments were performed at 1 Hz with -10% static predeformation at $25\text{ }^{\circ}\text{C}$ (Adapted with permission from Ref. [94], copyright 2002 Springer)

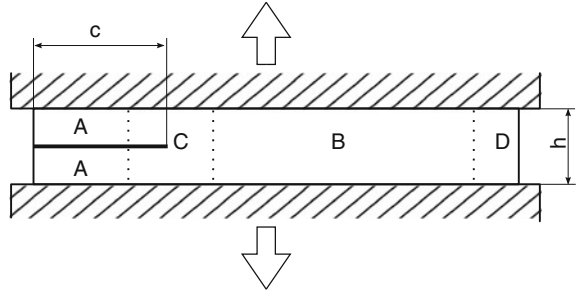
tear fatigue investigations in elastomers can be traced back to the 1940s with the introduction of synthetic rubbers [96, 97]. By definition, the prediction of fatigue life involves the steps of crack nucleation and growth [98, 99]. In the case of rubbers, the common assumption is that cracks propagate from inherently existing defects like filler agglomerates, additives like zinc oxide, impurities occurring naturally in the raw elastomer, and imperfections in mold surfaces [100]. For instance, it was found by SEM that the majority of the cavities contained a zinc oxide granule [101]. Mars even argued that crack nucleation in a narrow sense does not occur due to the presence of flaws [100].

In the early days of rubber fracture research, the Griffith criterion was used for brittle elastic materials, relating the strain energy stored in a notched material to the surface energy γ required to advance the crack. However, this simple concept is not applicable to rubbers, since the stored strain energy cannot be fully converted to surface energy due to dissipation effects [102]. In the 1950s, Rivlin and Thomas extended the energy-based Griffith criterion to elastomers [103, 104]. They introduced the critical energy release rate, which has become the most widely used concept in fracture mechanics of rubbers [104]. They showed that the critical energy release rate, above which the crack propagates, is independent of the sample geometry under certain conditions [97]. In the field of rubber technology, the term **tearing energy** is commonly used for the fracture mechanics expression **energy release rate** [97].

The energetic approach to fracture mechanics can be applied on a global and on a local scale [105]. Applying it globally, the calculation of the tearing energy depends on the geometry of the rubber specimen. Nowadays, the most popular geometry is the so-called **pure shear sample**,¹² because it gives the most accurate results due to inherently better statistics [106]. Other geometries, like the single edge notched

¹² The term *pure shear* might be somewhat misleading. Simply speaking, the pure shear specimen is a tensile specimen with one of its dimensions transversal to the tensile direction being much larger than its extension along the tensile direction, such that transversal strains are restricted to one

Fig. 1.8 Illustration of a tear fatigue experiment in pure shear geometry. Zone A is stress-free, zone B is in pure shear state, zones C and D are in complex states of stress due to crack tip and boundary effects. The arrows indicate the tensile direction. Adapted from Ref. [103]



tensile (SENT) sample or the trousers sample, are mainly of historical interest [97, 102, 106]. For a pure shear geometry, the tearing energy can easily be calculated from a global energy balance (Fig. 1.8) [103]. If we let the crack propagate by the distance dc perpendicular to the tensile direction, then the zone C expands in length by dc and zone B shrinks by dc , assuming a self-similar shift of the crack tip. As a first approximation, no change in displacement occurs during the crack growth, i.e. the process is static. Then the energy W transferred from zone B to zone C is

$$W = h t w_{el} dc = t T dc, \quad (1.12)$$

where h and t are the height and the thickness, respectively, of the specimen; and w_{el} is the elastic strain energy density in the homogeneously deformed zone C. T as the tearing energy follows as

$$T = h w_{el}. \quad (1.13)$$

The elastic strain energy density w_{el} can be obtained from the area under the equilibrium stress-strain curve (which more closely resembles the unloading curve than the loading curve) of an unnotched pure shear sample, possibly with some correction for boundary effects in the D zones. Alternatively, w_{el} is obtained from the strain in connection with a constitutive model. Strictly speaking, Eq. 1.13 is only valid under static conditions, i.e. no work is done on the sample while the crack propagates. To a good approximation, this is fulfilled in quasistatic tear tests, where the sample is stretched continuously and the crack growth is observed. However, these kinds of rupture tests can hardly represent the fatigue loading conditions which are typically encountered in rubber products. Moreover, performing quasistatic tear tests is meaningless for strain-crystallizing rubbers since catastrophic failure occurs once the crystalline zone, acting like a wall, has been overcome [6, 103, 107].

Besides the global approach, a local approach, based on the J -integral, is available. In simple words, this concept, proposed independently by Rice and Cherepanov [108, 109], performs a local energy balance around the crack tip. In analogy to

(Footnote 12 continued)

dimension. The name results from the fact that this deformation field can theoretically be obtained by exerting shear forces on the edges of the sample, along with a rotation of the sample [16].

Green's theorem, the energy components acting on and crossing an arbitrary closed path around the crack tip are summed up to obtain the energy source term within this area, which corresponds to the creation of new crack surfaces and energy dissipation. If dissipation occurs only in the crack tip near field, the J -integral approach becomes path-independent, provided it encircles the crack tip near field. When taking the sample contour as integration path, the J -integral reduces to Eq. 1.13 [110]. If dissipation is not limited to the crack tip near field, the J -integral becomes path-dependent. The analysis of crack propagation in dissipative materials of arbitrary geometry is subject to current research [111].

In practice, cyclic fatigue crack growth experiments are preferred over static tear tests, because they resemble more closely real-life loading conditions. In these so-called tear fatigue tests, the notched rubber specimen is subjected to a cyclic load at a frequency of roughly 1 Hz (pulsed or harmonic) and the crack growth over the number of cycles is observed (Fig. 1.9a).¹³ While at small strain amplitudes the growth is dominated by ozone attack (regime 1 in Fig. 1.9b) and at large amplitudes catastrophic failure occurs (regime 3), the region inbetween (regime 2) is characterized by a power law relation between the crack growth per cycle $\frac{dc}{dN}$ and the tearing energy T to the power of m :

$$\frac{dc}{dN} \propto T^m \quad (1.14)$$

The Paris law (Eq. 1.14) was originally established for metals [97]. m is an empirical parameter and is between 3 and 4 for NR and SBR, respectively [6, 112]. There are several limitations which are not captured by the Paris law. First, the fatigue life not only depends on the load amplitude, but also on the load frequency and load history. Under pulse load, resembling more closely the loading scenario in a tire, the lifetime can be considerably reduced as compared to sine load [113]. The extent of lifetime reduction depends on the compound, such that the material rankings from a sine and a pulse test can be completely different [114]. Also, the introduction of dwell periods or variable amplitude loading histories can drastically change the lifetime by up to factor of ten [115]. Literature does not give an unequivocal picture about the influence of the strain rate and frequency. While Andrews [116] and Gent [6] showed, somewhat counterintuitively, a negligible effect of frequency on crack growth in NR, recent results [113], varying only the strain rate and not the frequency, suggest a decrease in tear resistance with increasing strain rate. However, this could also be related to the inherent variation in dwell time when changing the strain rate at a constant frequency, which was shown to have a large effect [115, 117].

The most influential parameter besides amplitude and frequency is the R -ratio, defined as the ratio of minimum to maximum strain or strain energy in a fatigue cycle [104]. While in amorphous elastomers the R -ratio has a negligible effect [117], in strain-crystallizing NR the crack growth rate can decrease by as much as two orders of magnitude when the R -ratio is increased from 0 to 0.06 [99]. This is nicely

¹³ In the framework of the FOR 597 research group, tear fatigue experiment were carried out on a Coesfeld machine at TU Chemnitz.

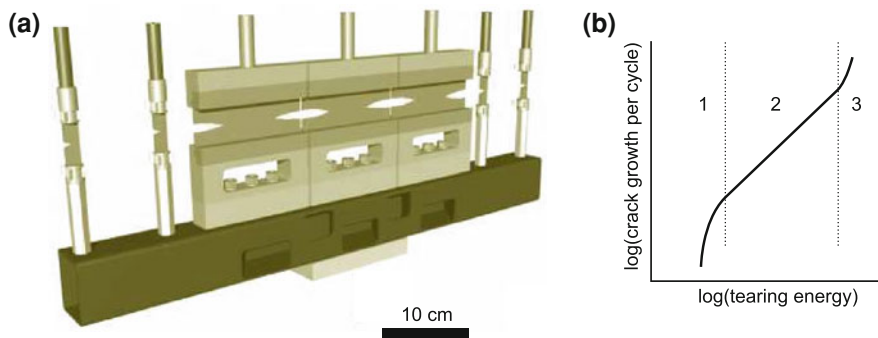


Fig. 1.9 Tear fatigue analysis: **a** Scheme of a tear fatigue analyzer for parallel testing of pure shear and SENT samples (image courtesy of R. Stoček, TU Chemnitz); **b** Illustration of fracture regimes in tear fatigue. 1 minimal crack growth due to ozone attack, 2 power law regime, 3 catastrophic failure (Adapted with permission from Ref. [118], copyright 2012 Springer)

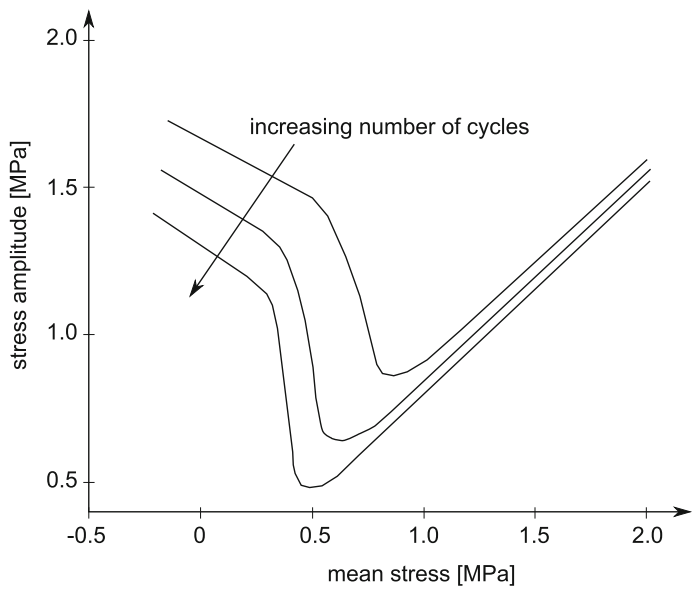


Fig. 1.10 Haigh diagram of filled natural rubber (23 phr carbon black) subjected to harmonic strain at 1 Hz. The criterion for the number of cycles listed in the graph is the presence of a crack larger than 1 mm. The characteristic of natural rubber is the increase of the isolines with increasing positive mean stresses (Adapted from Refs. [121] and [122])

reflected in the Haigh diagram (Fig. 1.10), plotting the stress range of a cycle, $\Delta\sigma$, over the average stress per cycle, $\bar{\sigma}$, which shows a characteristic increase in the isolines for constant lifetime [119], i.e. cycling around a larger strain increases the lifetime despite the higher strain energy density involved, which should theoretically release more energy and favor crack propagation. The reason behind this apparent

paradoxon is the strain-induced crystallization, which can develop its reinforcing abilities only when the material is kept above a certain strain for sufficient time. The relation between strain-induced crystallization and tear resistance was first pointed out by Busse in 1934 [120].

The role of SIC in crack growth is also apparent from the topographies of the crack contour and crack surface. In non-crystallizing rubbers or if SIC is suppressed (e.g. due to high strain rates), the crack surface is rather smooth [6]. The more prominent the role of SIC, the more wrinkled the surface becomes. Knotty tearing [123, 124] and characteristic striations [107, 116] result from the reinforcing crystalline zone at the crack tip and the anisotropy of the material in that region, forcing the crack to make a detour. Thus, on top of the large hysteresis associated with strain-crystallizing materials, the real crack surface is much larger than what a simple crack length measurement would suggest, effectively enhancing the apparent tearing energy, e.g. obtained from a pure shear tear fatigue test. Under certain circumstances, even crack rotation and bifurcation are observed in NR [62, 125], effectively increasing the crack tip radius and thus elevating the energy release rate [126]. A more detailed description of the role of SIC and its time dependency follows in Sect. 1.3.2.

The tear fatigue tests outlined above have in common that their loading conditions are limited to uniaxial cases, which contrasts real-life scenarios, frequently exhibiting multiaxiality [127]. Typically, the cracking plane is observed to be normal to maximum principal strain direction [100]. Various multiaxial equivalence fatigue criteria relate the tearing energy obtained from a uniaxial test to the actual strain and stress field under multiaxial conditions [98, 128]. This field is subject to current research [129].

Other factors affecting the fatigue lifetime include the crosslinking type and density [99, 130, 131], and the sample thickness [97, 132, 133].

1.2 X-Ray Scattering

X-ray scattering is a powerful non-destructive analytical technique to probe the nano- and microstructure of materials. Employed in transmission geometry¹⁴ it is bulk-sensitive and, depending on the setup, provides local information or averages over a large volume to yield representative results. X-ray scattering can have high time-resolution in the millisecond range, but can also follow slow processes. X-ray scattering can be done with ease in rather flexible sample environments, e.g. in-situ heating, cooling or mechanical experiments can be implemented.

The data obtained are strictly quantitative, however its interpretation is the main difficulty and drawback of this method. Scattering data represents information in reciprocal space, which is hardly accessible to common human perception, and therefore either a conversion into real space, whether direct or by modeling, has to be done, or, on the assumption of certain geometries, a direct extraction of information from reciprocal space can be performed.

¹⁴ As opposed to grazing incidence geometry.

1.2.1 Nature and Sources of X-Rays

X-rays are electromagnetic radiation, which are located at the high energy end of the electromagnetic spectrum. Their wavelength λ ranges from 0.01 to 10 nm, corresponding to energies between roughly 100 and 0.1 keV. X-rays were discovered in 1895 by Wilhelm Conrad Röntgen.

The most widely used source of X-rays is the X-ray tube, which emits X-rays from a target (typically copper), that is bombarded with electrons. The electrons are emitted from a cathode wire and are being accelerated by an electric voltage. Besides the Bremsstrahlung background, an X-ray tube emits radiation of a few characteristic wavelengths, which result from electrons from distinct outer shells falling down into the vacancies in the inner shell caused by the electron bombardment (fluorescence). For instance, the most frequently used type of radiation in X-ray scattering, Cu $K\alpha$ radiation, is caused by a transition of electrons from the L-shell to the K-Shell and has a wavelength of 0.154 nm.

The major disadvantage of the X-ray tube is the low efficiency, which is mainly due to the isotropic emission of X-rays from the target. Because a defined beam is required for scattering purposes, only a small portion of the radiation can be used. The low photon flux leads to long exposure times to yield a sufficient signal to noise ratio. This renders time-resolved experiments and high-throughput measurements impossible.

A more powerful alternative is the synchrotron light source (Fig. 1.11). In a synchrotron, electromagnetic radiation is generated from the deflection of charged particles (electrons or positrons) moving at relativistic speeds. The first of these large-scale facilities were built in the 1960s to perform particle physics experiments, and the electromagnetic radiation was only a byproduct. Nowadays, with the third generation of synchrotron sources being available, they are purposefully designed to deliver high brilliance¹⁵ X-ray radiation.

In a synchrotron source, electrons or positrons are accelerated by a linear accelerator and booster and then fed into a storage ring, typically of a few hundred meters in diameter. The particles circulate in the storage ring at relativistic speeds. Being at energies around 5–8 GeV, $1 - \frac{v}{c} \approx 10^{-5}$ (with v being the particle speed and c being the speed of light). In the storage ring, bending magnets force the electrons to move in a circle. The deflection of charged particles causes radiation loss, which is emitted as X-rays. The loss of energy is compensated by acceleration cavities. Besides the bending magnets, other devices (wigglers and undulators) are purposefully inserted into the storage ring to generate more brilliant radiation. Wigglers can be regarded as periodic arrays of n bending magnets, such that the brilliance is $\frac{n}{2} \approx 100$ times higher than that of a bending magnet. Undulators, employed in 3rd generation synchrotrons, are designed similarly as wigglers, but take advantage of amplification effects by interferences between the emitted X-rays from individual magnets, such that their brilliance is again enhanced by two to three orders of magnitude.

¹⁵ The brilliance is the photon flux (i.e. photons per time and per beam cross sectional area) normalized by solid angle (cf. beam divergence or collimation) and 0.1 % bandwidth (cf. monochromaticity).

Fig. 1.11 Aerial view of the Petra III storage ring and the Max-von-Laue experimental hall (blue) at DESY, Hamburg. It houses the MiNaXS beamline, at which most of the experiments for this work were carried out (Reproduced with permission from Ref. [134], copyright DESY, Reimo Schaaf)



After the X-ray beam has left the storage ring in tangential direction, it passes through some optical devices, which focus the beam (by means of a Göbel mirror or by slits) and confine the wavelength spread of the beam (only waves within a certain wavelength window fulfill the diffraction conditions of the monochromator crystals) and finally arrive at the experimental hutch of the beamline.

The difference in brilliance between a rotating anode lab source and the latest synchrotron sources is more than ten orders of magnitude. This high brilliance is especially useful for USAXS and SAXS. Considering that for WAXD the intensity itself is more relevant, still the exposure times at a synchrotron are reduced by a factor of 10^5 as compared to lab experiments, opening up new methods to study processes on previously inaccessible short time scales.

1.2.2 Scattering and Diffraction

This section deals with X-ray scattering and diffraction as analytical techniques in materials science to probe the nano- and microstructure of polymers. It intends to give a moderately detailed introduction into the theoretical fundamentals of the method, sufficient to understand and interpret experimental and literature data. The section should not be seen as attempt to comprehensively cover the theory of electromagnetic fields or quantum mechanics to deduce scattering theory from first principles.

Along these lines we start with the experimental setup and from there illustrate the physical relations. The theory laid out in the following is based on the classical books by Guinier [136], Feigin and Svergun [137], Glatter and Kratky [138] and a recent publication by Lindner and Zemb [139]. Figure 1.12 shows a sketch of a scattering experiment. Let us assume the incoming beam is a monochromatic planar wave, linearly polarized in the plane of the paper, i.e. the electric field vector points out of the plane of the paper. The electric field of the photon produces an oscillation of electric charges in the sample. As a good approximation, we can neglect the interaction

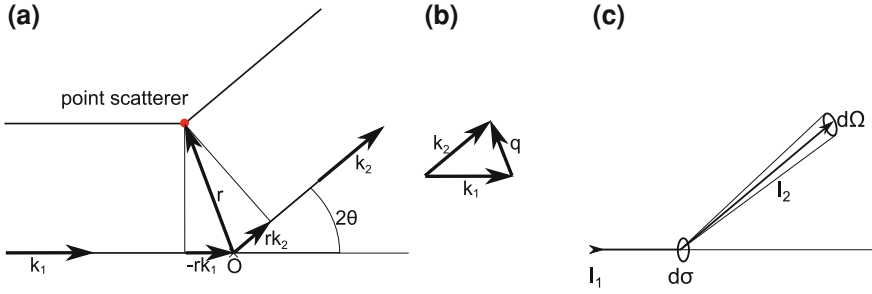


Fig. 1.12 **a** Schematic representation of a scattering experiment. **b** Graphical definition of the scattering vector \mathbf{q} . **c** Illustration of the scattering cross section $\frac{d\sigma(\mathbf{q})}{d\Omega}$ (Adapted from Ref. [135])

between X-ray photons and protons due to their large mass.¹⁶ An oscillating electron emits an electromagnetic wave. Assuming elastic scattering ($\lambda_2 = \lambda_1$), the relation between the scattered wave \mathbf{E}_2 and the incoming wave \mathbf{E}_1 is

$$\mathbf{E}_2 = \mathbf{E}_1 \frac{e_0^2}{m_0 c^2 r} \exp(-i\mathbf{q}\mathbf{r}), \quad (1.15)$$

where $r_0 = \frac{e_0^2}{m_0 c^2}$ is the electron radius, \mathbf{r} is the position of the electron and \mathbf{q} is the **scattering vector** $\mathbf{q} = \mathbf{k}_2 - \mathbf{k}_1$ (Fig. 1.12a, b).¹⁷ The magnitude of the scattering vector is, with $|\mathbf{k}_1| = k_1 = \frac{2\pi}{\lambda}$,

$$q = 2k_1 \sin(\Theta) = \frac{4\pi}{\lambda} \sin(\Theta). \quad (1.16)$$

The amplitude of the scattered beam relates to the amplitude of the incoming wave via the electron radius r_0 , which is the **scattering length** of a single free electron.

X-ray detectors can only detect the intensity of photons (in terms of counts per time and area, within a certain energy range), not their phase. The relation between amplitude E and intensity I is in the far-field approximation (i.e. the scattered spherical wave is approximated as a plane wave)

$$I(\mathbf{q}) = \frac{\epsilon_0 c}{2} \mathbf{E}(\mathbf{q}) \mathbf{E}^*(\mathbf{q}) \propto E^2(\mathbf{q}), \quad (1.17)$$

where ϵ_0 is the dielectric constant and \mathbf{E}^* is the complex conjugate of the amplitude \mathbf{E} . This brings us to the definition of the **differential scattering cross section** (Fig. 1.12c) $\frac{d\sigma(\mathbf{q})}{d\Omega}$:

¹⁶ Following Eq. 1.15, the amplitude of a wave scattered by a proton is $\left(\frac{m_p}{m_0}\right)^2 = 3.37 \times 10^6$ times less than the amplitude of a wave scattered by an electron.

¹⁷ For a detailed derivation of Eq. 1.15, the reader is referred to Berne and Pecora [140].

$$I_1 d\sigma(\mathbf{q}) = I_2(\mathbf{q}) l^2 d\Omega, \quad (1.18)$$

with Ω being the solid angle and l being the distance between the scatterer and the detector (detecting a wave of intensity I_2).

So far we considered scattering from a single free electron. In the context of scattering, an atom can be viewed as an assembly of electrons. For classic scattering experiments, anomalous effects (i.e. inelastic interactions due to the energy levels of the binding electrons) and multiple scattering events can be neglected. Then the scattering intensity of an atom, called the **atom form factor**, F_{atom} , is approximately proportional to its atomic number, Z :

$$F_{\text{atom}}(\mathbf{q}) = \int_{\text{atom}} \rho(\mathbf{r}) \exp(-i\mathbf{q}\mathbf{r}) d\mathbf{r} \propto Z, \quad (1.19)$$

where $\rho(\mathbf{r})$ is the electron density distribution within the atom.¹⁸ Equation 1.19 shows that the atom form factor is the Fourier transform of the electron density distribution. Combining Eqs. 1.15, 1.17 and 1.19, we obtain for the scattering intensity $I(\mathbf{q})$ of a hypothetical sample consisting of N uncorrelated atoms:

$$I(\mathbf{q}) \propto N F_{\text{atom}}^2(\mathbf{q}). \quad (1.20)$$

1.2.3 Small-Angle X-Ray Scattering

Small angle scattering comprises scattering at angles 2Θ well below 10° , i.e. structures in the range of 1–500 nm are analyzed, corresponding to scattering vectors $0.01 \text{ nm}^{-1} < q < 5 \text{ nm}^{-1}$. The low scattering angle end of this range is commonly referred to as USAXS (ultra ~), and the large-angle side at the boundary to WAXS is sometimes called MAXS (medium ~) [33, 139]. In other words, SAXS is sensitive to inhomogeneities in the scattering length density on the size scale of tens of nanometers. Thus we are not concerned about the electron density distribution within atoms, but rather about the distribution of phases or components of different electron density within the sample.

In analogy to the atom form factor, one can define particle form factors as the Fourier transform of the electron density distribution within the particulate structure. For instance, the **form factor** of a homogeneous sphere of radius R reads [139]:

$$f_{\text{sphere}} = 3 \frac{\sin(qR) - qR \cos(qR)}{(qR)^3}. \quad (1.21)$$

¹⁸ Other definitions exist in literature, taking the form factor as the square of the definition in Eq. 1.19.

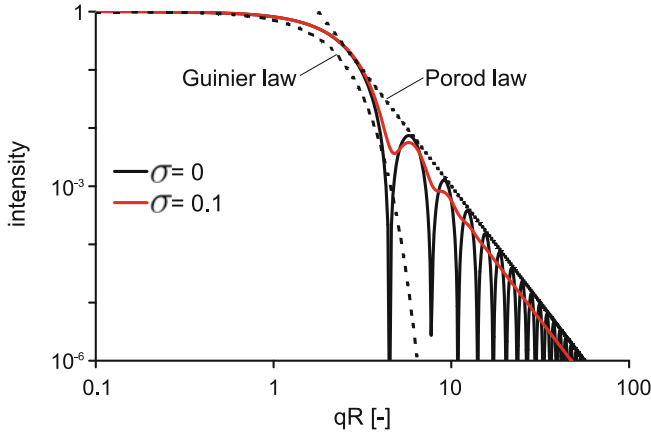


Fig. 1.13 Form factors of a monodisperse ($\sigma = 0$) and polydisperse ($\sigma = 0.1$) sets of spheres of radius R . A normal distribution with mean $qR = 1$ and standard deviation σ was assumed. The computed range is $0.05 < qR < 2.0$. With increasing polydispersity, the oscillations are blurred out. The Guinier and Porod laws are shown to hold at low and high qR , respectively

A computed scattering curve for a dilute system of spheres is shown in Fig. 1.13. For a number of other geometrically simple particles, the form factors can be computed numerically.

In a dilute solution of particles, interaction between the particles is negligible, and the scattering intensity is simply the sum of the scattering intensities of the individual particles.¹⁹ If, however, the particles interact, i.e. the average interparticle distance is of the same order of magnitude as the particle size, crossterms arise and give way to the introduction of a **structure factor** $S(q)$:

$$I(q) \propto V_p F(q)^2 S(q), \quad (1.22)$$

with V_p being the particle volume fraction. Consequently, for dilute systems, the structure factor $S(q)$ reduces to unity.

While the interpretation of scattering patterns in terms of form and structure factors requires an a priori model of the particle shape and interaction, model-free approaches are available. Considering that the scattering intensity is proportional to the square of the Fourier transform of the real-space electron density distribution (Eq. 1.20), one can go in the reverse direction and go from scattering space (also called s -space or reciprocal space) to real space by performing an inverse Fourier transform. Due to the phase problem, the recovery of the electron density distribution is impossible.²⁰ Instead, one obtains the **correlation function** $\gamma(r)$:

¹⁹ Dispersions with a particle volume fraction below 1 % are typically considered dilute [139].

²⁰ Theoretically, the complete real space information can be restored under certain conditions if the coherence time of the incident beam is long relative to the exposure time. This is part of the motivation behind the development of X-ray free electron lasers (XFEL).

$$\gamma(\mathbf{r}) = \mathcal{F}^{-1}(I(\mathbf{q})). \quad (1.23)$$

One also arrives at the correlation function by inserting Eq. 1.15 into Eq. 1.17:

$$I(\mathbf{q}) \propto \int_{\mathbf{V}} \rho(\mathbf{r}_1) \exp(-i\mathbf{q}\mathbf{r}_1) d\mathbf{r}_1 \int_{\mathbf{V}} \rho(\mathbf{r}_2) \exp(i\mathbf{q}\mathbf{r}_2) d\mathbf{r}_2 \quad (1.24)$$

With $\mathbf{r} = \mathbf{r}_1 - \mathbf{r}_2$, it follows:

$$I(\mathbf{q}) \propto \int_{\mathbf{V}} \int_{\mathbf{V}} \rho(\mathbf{r}_1) \rho(\mathbf{r}_1 - \mathbf{r}) \exp(-i\mathbf{q}\mathbf{r}) d\mathbf{r}_1 d\mathbf{r}, \quad (1.25)$$

where the correlation function $\gamma(\mathbf{r})$ can be identified as the autocorrelation of the electron density distribution:

$$\gamma(\mathbf{r}) = \int_{\mathbf{V}} \rho(\mathbf{r}_1) \rho(\mathbf{r}_1 - \mathbf{r}) d\mathbf{r}_1. \quad (1.26)$$

Instructive illustrations regarding the interpretation of the correlation function can be found e.g. in Refs. [33] and [141].

Other functions have been derived from the correlation function γ , following the principle of edge enhancement. The **interface distribution function (IDF)** is the second derivative of the one-dimensional correlation function; and the **chord distribution function (CDF)** is the three-dimensional equivalent of the IDF, mainly useful for anisotropic materials, obtained from the Laplacian of the three-dimensional correlation function [33]. These model-free approaches have certain limitations. First, to perform a Fourier transform, the experimental data is required to cover the complete reciprocal space. This of course is not feasible in practice. Scattering data for $\mathbf{q} \rightarrow 0$ has to be extrapolated. Merging data from different detector distances is advisable to cover a broader \mathbf{q} -range. Because a SAXS pattern only represents a slice of the reciprocal space, the reciprocal space in all three dimension can only be reconstructed under certain conditions. Either the sample fulfills fiber symmetry around an axis perpendicular to the X-ray beam, or the sample has to be rotated, which then requires a computationally expensive postprocessing of the data. The interpretation of a SAXS pattern, either directly or in real space representation, is greatly exacerbated by polydispersity and diffuse boundaries, i.e. gradual changes in electron density. Both issues are present in the systems studied in this work. The **Magic Square** gives a nice overview of the relations between real and reciprocal space (Fig. 1.14) [33].

An alternative approach is to postulate a structure in real space, based on direct interpretations of the scattering data, or based on the model-free approaches outlined above, or following other assumptions. Since the transformation from real space to reciprocal space is unequivocal, the scattering patterns can either be computed numerically or even analytically (in the case of simple geometries, cf. Eq. 1.21). Then the computed pattern is compared to the experimental one and the process

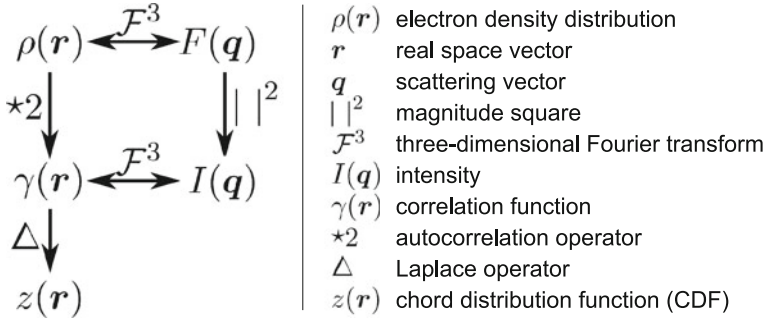


Fig. 1.14 Magic square to illustrate the relations between real space and reciprocal space functions (Adapted from Ref. [33])

is iterated until sufficient agreement is achieved. However, the obtained real-space structure is not unique.

For the special case of mass and surface fractals, the relations outlined in Sect. 1.1.3 hold.

Even though they can rarely provide a quantitative and precise evaluation of scattering data, some important very basic interpretations should be mentioned here. Historically, the Guinier law and the Porod law are of great importance. They still serve as a first rough guide in the visual interpretation of scattering curves. The **Guinier law** (Guinier 1939) holds for small q ($q \ll R_{g,e}$) and represents the outcome of the first term of a Taylor series expansion of the scattering intensity of isolated, monodisperse, spherical particles²¹:

$$I(q) \propto \exp\left(-\frac{q^2 R_{g,e}^2}{3}\right), \quad (1.27)$$

where $R_{g,e}$ is the electronic radius of gyration. In a Guinier plot, $\log(I)$ is plotted over q^2 and $R_{g,e}$ can be obtained from the slope of the curve. While the Guinier regime is seen as a distinct knee in a classic $\log(I)$ versus $\log(q)$ scattering curve (Fig. 1.13) and the position of the knee allows first conclusions regarding $R_{g,e}$, this feature is often blurred out by polydispersity or completely obscured due to concentration effects [142, 143].

At large q ($q \gg R_{g,e}$, large in the context of small-angle scattering, i.e. inhomogeneities in the electron density on the scale of nanometers), the **Porod law** (Porod 1951) holds:

$$I(q) \propto \frac{S_V}{q^4}, \quad (1.28)$$

²¹ For a derivation, see e.g. Guinier [136].

with S_V being the specific surface. Porod's law holds for well-defined smooth surfaces. If the density changes gradually or the surface is rough, the exponent deviates from 4 (cf. Sect. 1.1.3).

As pointed out above, scattering is the result of inhomogeneities in the electron density. Not only the shape of the scattering curve deserves interpretation, but also the absolute intensity of the scattering signal allows conclusions with respect to the structure. The better the contrast between the phases (i.e. the larger the difference in electron density), the higher the **absolute scattering intensity** Q . Owing to the fact that this quantity is independent of the shape of the scatterers, it is also termed **scattering invariant**. For a two-phase system, it reads

$$Q = \int \int \int_{q' \rightarrow 0}^{q' \rightarrow \infty} I(\mathbf{q}) \, d\mathbf{q} \propto \Phi_1 \Phi_2 (\rho_1 - \rho_2)^2. \quad (1.29)$$

Φ_1 and Φ_2 are the volume fractions of phases 1 and 2, respectively, and ρ_1 and ρ_2 are their electron densities. The fact that Q is insensitive to the inversion of the volume fractions is called **Babinet's principle**. Since the detector plane only provides a slice through the reciprocal space, the missing third dimension has to be taken from symmetry considerations or from rotating the sample to explore the complete reciprocal space. For systems with three or more phases, the equation becomes increasingly complex [144, 145].

1.2.4 Wide-Angle X-Ray Diffraction

Wide-angle X-ray diffraction follows the same physical phenomena detailed in Sect. 1.2.1. However, the regular periodic order of scatterers gives rise to interference peaks, called diffraction.²² The regular order on the size scale probed by WAXD ($\Theta > 10^\circ$) corresponds to the lattice spacing d in crystalline polymers. In order to observe constructive interference between scattered waves, the phase shift between the two incoming wavelets in Fig. 1.15 must be multiples of the wavelength [147]:

$$m\lambda = 2d \sin(\Theta), \quad (1.30)$$

where m is the order of diffraction.²³ Equation 1.30 is called **Bragg's law**. It simplifies the scattering problem to a planar case. For the three-dimensional case it is instructive to think in reciprocal space. In the special case of an orthorhombic crystal structure, like in NR, the base vectors of a unit cell of the **reciprocal lattice** are collinear with the lattice unit vectors in real space. Only their lengths are inverted. In order to fulfill the diffraction condition for a given crystallographic plane, the scattering vector

²² For an overview of diffraction theories, see e.g. Ewald [146].

²³ In polymer science, higher order diffraction peaks are frequently concealed due to imperfections and finite size effects.

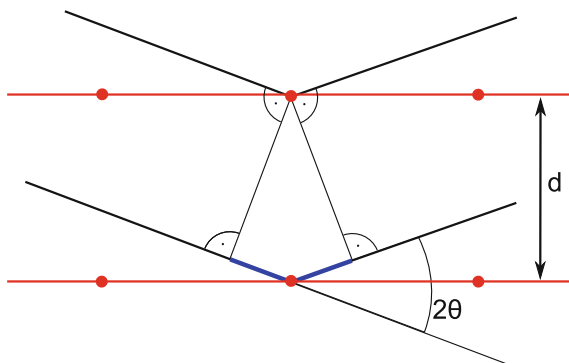


Fig. 1.15 Illustration of the diffraction condition. The *red lines* represent the crystal lattice; the *black lines* represent the X-ray photon paths. To fulfill Bragg's law, the *blue line* must be of length $m\lambda$

\mathbf{q} must be equal to the corresponding reciprocal lattice vector. This mathematical relation is geometrically expressed in the **Ewald sphere** construction. In line with Fig. 1.15, diffraction occurs when a lattice point lies on the Ewald sphere, which is defined by its center O being at \mathbf{k}_1 and its radius $|\mathbf{k}_1| = \frac{2\pi}{\lambda}$ (Fig. 1.16). For a detailed derivation of the Ewald sphere construction see e.g. Ref. [148].

In numerous scattering and diffraction experiments in polymer science, advantage is taken of the **fiber symmetry** of the sample. This means that the sample structure is symmetric to a rotational axis. In particular, in a uniaxial tensile experiment, the symmetry axis coincides with the tensile axis, as long as the two transversal dimensions of the sample are similar. When fiber symmetry is fulfilled, we can replace the reciprocal lattice by an infinite number of lattices sharing the rotational axis, which is the c -axis in the case of NR. Or, if we stick with one lattice, the reciprocal lattice point does not need to lie on the Ewald sphere any more; instead, it is sufficient if the distance of the reciprocal lattice point from the axis of fiber symmetry equals k_1 .

As opposed to metals, crystallizing polymers never become completely crystalline due to steric hindrance and due to entropy reasons [149]. Common degrees of crystallinity for semicrystalline polymers range between 10 and 70 % maximum. The remainder stays amorphous, which gives rise to the so-called amorphous halo in the wide-angle regime. The degree of crystallinity is reflected in the diffractogram as the ratio of the intensity of the crystalline diffraction peaks to the intensity of the amorphous halo [33, 150–152]. However, this method only yields a relative number for the crystallinity, such that a normalization with independent measurements (DSC or dilatometry) is required. Alternatively, one can evaluate the decrease in the amorphous halo for itself [86, 153, 154]. An overview of methods for the determination of crystallinity is listed in Ref. [155].

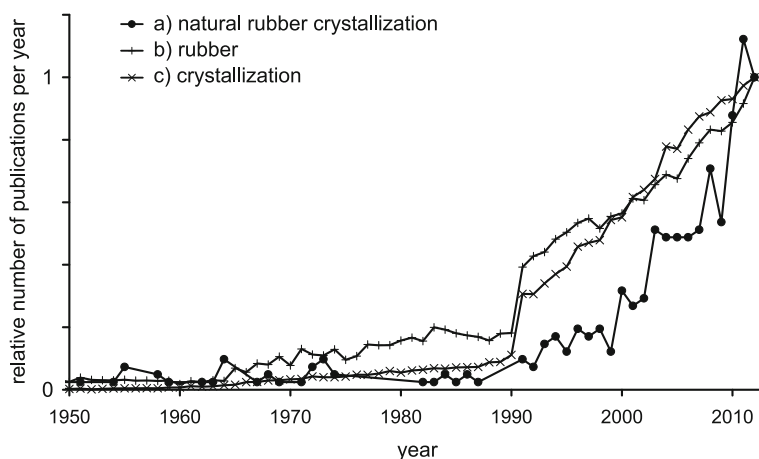


Fig. 1.17 Number of publications per year assigned to the topic of (a) *natural rubber crystallization* according to the Web of Knowledge. Given that the total number of publications per year increases continuously in almost all fields, only a careful look at the slope of the increase can identify research fields gaining importance. Thus, for comparison, the search for the keywords (b) *rubber* and (c) *crystallization* is shown. All data is normalized with respect to the 2012 figures. Total number of papers for (a) is 401, for (b) is 48347, for (c) is 128696. The rise in (a) since 2000 is very prominent and is not observed in (b) and (c). As of May 14, 2013

1.3 Crystallization in Natural Rubber

1.3.1 General Aspects of Crystallization in Natural Rubber

The earliest studies of structural changes in rubbers under strain date back to the 1920s, when Katz published his report on strain-induced crystallization²⁴ in natural rubber observed by WAXD [156]. Even though the fundamentals of macromolecular chemistry were still lacking at that time, he concluded that highly stretched natural rubber consists of two phases and that the phase transition is reversible when the strain is removed. Since the early 2000s, the number of papers dealing with SIC has been increasing owing to the availability of more powerful synchrotron sources (Fig. 1.17). SIC attracts so much attention in the research community because it makes a big contribution to the outstanding properties of NR (Sect. 1.1.4.4). Natural rubber crystallizes in an orthorhombic²⁵ unit cell with lattice dimensions $a = 1.24$ nm, $b = 0.88$ nm, $c = 0.82$ nm [157–161]. A unit cell, containing two mers of cis-1,4 polyisoprene, is shown in Fig. 1.18.

Considering crystallization in natural rubber, one has to distinguish strain-induced crystallization (SIC) and thermal (quiescent) crystallization (TIC) [162]. Unde-

²⁴ Katz called it *fibering* what is now termed *strain-induced crystallization*.

²⁵ Some dispute exists in literature about the precise value of the β angle, taking values up to 93° , suggesting a monoclinic unit cell.

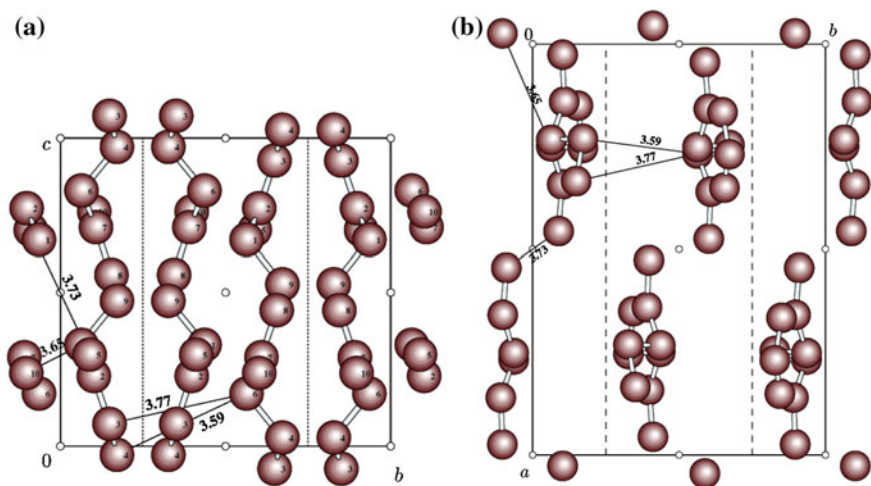


Fig. 1.18 Unit cell of crystalline natural rubber. **a** view along the a -axis on the bc plane; **b** view along the c -axis on the ab plane (Adapted with permission from Ref. [158], copyright 2005 American Chemical Society)

formed natural rubber undergoes significant thermal crystallization at temperatures below $0\text{ }^{\circ}\text{C}$ with a maximum crystallization rate around $-28\text{ }^{\circ}\text{C}$ [16, 163]. The thermodynamic melting point lies considerably above $0\text{ }^{\circ}\text{C}$ [80, 164]. With increasing strain, the melting temperature increases [60]. At room temperature, SIC sets in at a strain of roughly 300 % in unfilled natural rubber [165]. Above $70\text{ }^{\circ}\text{C}$, no SIC is observed [60]. It should be noted that, despite having the same crystal structure, the morphologies of thermally induced crystallites and strain induced crystallites are completely different [166, 167]. Quiescent crystallization forms spherulites [168, 169], whereas SIC promotes the formation of highly oriented fibrillar structures (Fig. 1.19) [167, 170]. In spherulites, folded-chain lamellae are arranged isotropically, giving rise to an unoriented WAXD pattern [171]. The periodic spacing (long period) of the lamellae can be inferred from the long period ring position in a SAXS pattern [169, 172]. The long period is in the range of 20 nm, depending on temperature [169]. In contrast to TIC, strain-crystallized NR contains semicrystalline strands, highly oriented along the stretching direction. These strands are made up of small extended chain crystallites, interrupted by amorphous segments due to entanglements and crosslinks, which cannot be transformed to the crystalline state. The strands are roughly 10–25 nm in diameter [173]. Historically, these crystallites were called γ -fibrils by Andrews, and are now generally referred to as shish [162, 174, 175]. Cooling of strain-crystallized NR can produce intermediate structures, depending on the strain and temperature. In this case, the shish serves as a backbone for lamellar overgrowth, forming folded-chain α -crystallites (or kebab) perpendicular to the backbone [174].

In the following, only SIC is considered.

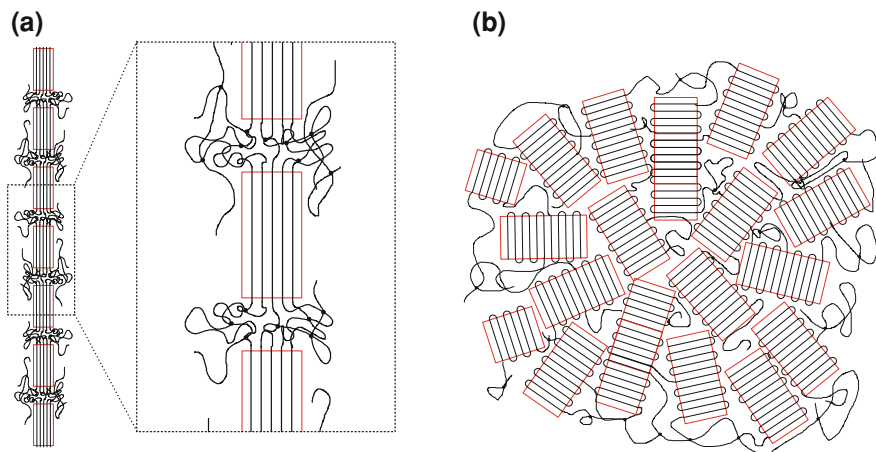


Fig. 1.19 Crystal morphologies in semicrystalline NR. **a** Shish structure resulting from strain-induced crystallization. Stretching direction is vertical. **b** Spherulitic morphology from thermal quiescent crystallization. For simplification, the chains are drawn with adjacent re-entry. In both cases, entanglements and crosslinks are restricted to the amorphous phase

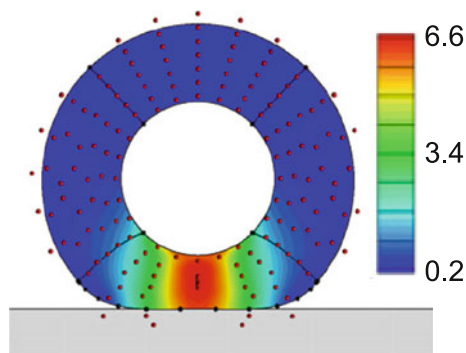
While SIC can be analyzed by a range of methods, e.g. DSC [176, 177], NMR [60, 175], IR spectroscopy [175] and dilatometry [176], the most widely used method is WAXD. The relations between strain, temperature and crystallinity have been studied extensively [178].

At first sight, the fact that in unfilled rubber the SIC sets in at strains as large as 300 %, suggests that SIC might be of little relevance in real-life loading conditions of most rubber products. However, in reality the local strain often considerably exceeds the nominal strain. In filled rubbers, due to the rigidity of the filler phase, the matrix phase has to bear the complete deformation, such that the matrix strain is considerably larger than the external strain, especially when the rubber is highly filled. This effect is referred to as strain amplification (Sect. 1.1.4). Thus, in filled rubbers, the SIC onset strain can be reduced to around 150 % strain. Second, certain geometries give rise to local strain concentration, e.g. around a crack tip. Theoretically, when approaching a crack tip, one encounters a strain singularity. In reality, the local strain concentration leads to a crystalline zone around the crack tip which locally reinforces the material and thus slows down the crack growth.

1.3.2 Kinetics of Crystallization

Besides the effects of strain and temperature, the time-dependency of SIC should not be overlooked. Since most rubber products, especially tires, are subjected to dynamic loads, the structure under realistic loading conditions can considerably

Fig. 1.20 Stress distribution in an idealized tire in contact with a rigid surface. The *color index* represents the magnitude of the first Piola-Kirchhoff stress tensor. In a rolling tire, a given material voxel experiences a pulse-like stress history (Adapted with permission from Ref. [183], copyright 2011 Elsevier)



deviate from what is suggested by quasistatic experiments (Fig. 1.20). This is due to the finite crystallization kinetics and was shown for the first time in 1932 by Acken et al., who utilized a stroboscopic technique to accumulate WAXD diffractograms over several deformation cycles to reach sufficient exposure [179]. They found that the crystallinity in the dynamically stretched rubber was considerably suppressed as compared to quasistatic experiments. This type of setup was later optimized by Kawai et al. [180, 181]. Using a variable phase shift between the stroboscope and the dynamic stretching device, the complete crystallinity versus strain curve could be reconstructed. Recently, Candau et al. extracted a crystallinity versus time curve from stroboscopic dynamic experiments [182]. They defined the characteristic time as the time period between the onset of crystallization and the time at maximum strain in a cyclic experiment. By varying the stretching frequency, they constructed a crystallinity versus characteristic time plot, which was fitted with a stretched exponential function. They obtained a characteristic crystallization time of 20 ms.

The alternative approach to cyclic loading is to apply a steplike loading and then to follow the crystallization over time. The pioneering work in this respect was done by Dunning and Pennells in 1967, who took advantage of a continuous steplike strain when a rubber band is passed over two rolls rotating at different speeds [184]. They reported incubation times between 5 ms and 18 s, depending on the strain level. However, the fact that the initial scattered intensity in the region of the diffraction spots increases with strain, suggests that crystallization might have set in even at times shorter than the experimental time scale.

Mitchell and Meier performed experiments on a high-speed tensile tester. They utilized the enthalpy of crystallization and employed thermal techniques to measure the crystallinity after a steplike loading [185]. This method relies on several assumptions in order to separate crystallization enthalpy from the work of deformation. The crystallinity versus time behavior was fitted with a first order rate law with a half time of 45 ms.

Only in the last few years, owing to the availability of more powerful synchrotrons, did the direct measurement of crystallinity after a step strain become possible. Tosaka et al. performed WAXD experiments with a pattern acquisition rate of approximately

12 Hz [8, 186, 187]. Despite relatively slow steplike loading (usually 10 s^{-1}), they reported that the crystallization process only begins after the loading step is finished, following a two-step kinetic law. After roughly 10 s the crystallinity was found to approach a steady state.

To date, the understanding of the molecular processes and mechanism behind the crystallization kinetics is still very limited. An interpretation of strain-induced crystallization on the molecular level, e.g. in analogy to the well-known nucleation and growth models for quiescent crystallization, is still lacking [188]. In that sense, the SIC theory lags behind the TIC theory by several decades. De Gennes put forward the idea of an instantaneous coil-stretch transition [189]. Later Hsiao et al. proposed to apply this transition to chain segments between crosslinks [190], considering that the crystallites are much smaller than the typical distance between crosslinks or entanglements, which is of the order of 20–150 nm [10, 191, 192].

In the context of thermal crystallization, the most famous kinetic equation is the Avrami equation [193]. It has been modified and extended since its introduction in the 1940s. However, it only considers the superstructure of the crystallites on the level of the ordering of lamellae into spherulites and the growth of the spherulites. It does not address the transition from the random coil state to lamellae. Therefore, it is not applicable to SIC.

1.4 Cavitation

It is commonly accepted that the presence of cavities²⁶ in deformed rubber interferes with the mechanical behavior of the material. On the one hand, the energy dissipation involved in the formation of cavities toughens the material. On the other hand, cavities can impair the mechanical properties and the growth of cavities is considered to play a major role in the early stages of crack propagation [101, 194–197]. Due to its long history and due to the importance of the subject, it has been reviewed several times [194, 198, 199].

The most widely used method to detect cavitation is dilatometry during deformation [163, 176, 200–203]. It was pointed out that due to the diffusion properties of rubber, gas dilatometers cannot be used to determine cavitation [176]. Also the superposition of volume changes by cavitation and strain-induced crystallization has to be accounted for. SIC leads to a decrease in volume by up to 2.7 % [163]. Another popular method is scattering [144, 145, 204, 205], either from X-rays or light. Due to the large difference in electron density between the cavities and the surrounding matrix, cavitation is reflected in a strong increase in total scattering intensity. The presence of elongated cavities is observed as a streak in the scattering pattern. The disadvantage of scattering methods is that they can only detect cavities within a certain narrow size range. Recently, optical methods gained popularity as a method

²⁶ The terms *cavitation* and *void formation* are often used interchangeably, however some authors prefer to use *voids* to describe stable hollow regions in thermoplastics and other glassy materials, whereas *cavities* is used in the context of elastomers for hollow regions growing in an unstable manner [194].

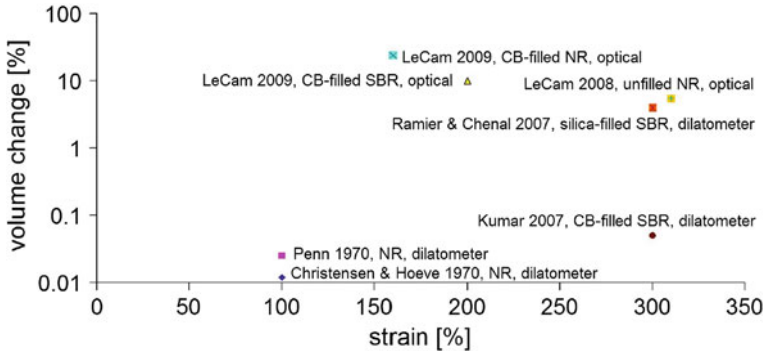


Fig. 1.21 Literature overview of volume changes in elastomers under strain, measured by various methods and on different materials. Le Cam 2008 [208], Le Cam 2009 [207], Ramier and Chenal 2007 [205, 213], Kumar 2007 [218], Penn 1970 [201], Christensen and Hoeve 1970 [200]

for volume measurement [206–208]. Furthermore, cavitation was studied by SEM [101, 209], tomography [210], acoustic emission analysis [211] and NMR [197].

Despite the multitude of investigations, no clear picture about the quantity of cavitation could be obtained so far (Fig. 1.21). However, most reports agree that in unfilled rubber, cavitation is negligible [200–202, 205, 212]. Few authors reported a significant volume increase in unfilled rubber [207, 208, 213], which might be ascribed to the high zinc oxide content in the *unfilled*²⁷ samples under study. For filled rubbers, most studies reported volume increases between 1 and 5% [176, 200, 202, 205, 213], whereas LeCam found a volume increase by as much as 25%.²⁸ The results suggest that cavitation is more prominent when filler loadings are high, the adhesion between filler and matrix is low and the strain is large [205, 209, 214].

The mechanical criteria for cavitation are still subject to discussion. The most famous approach is due to Gent (1958), who argued that the critical stress is $\frac{5}{6}E$, with E being the tensile modulus [215]. Despite the good agreement with experimental results, he later noted that this simple relation only holds for a certain limited particle size range [144, 199, 216, 217]. A different approach follows the Griffith criterion in the derivation of a cavitation criterion [194]. It supports experimental evidence that a certain minimum initial flaw size is required in order to expand the flaw to a cavity. It is commonly assumed that defects of a size larger than 100 nm exist in any rubber material, such that the cavitation problem can be reduced to the growth of these defects.

²⁷ *Unfilled* typically specifies materials without reinforcing filler. Recipes containing additives like zinc oxide are thus classified as *unfilled*.

²⁸ It should be noted that the rubbers studied by LeCam contained the unusually high amount of 10 phr of zinc oxide, which possibly stimulates cavitation.

References

1. J. Loadman, *Tears of the Tree: The Story of Rubber—A Modern Marvel* (Oxford University Press, Oxford, 2005)
2. A. Hwee, Y. Tanaka, Structure of natural rubber. *Trends Polym. Sci. (Oxford)* **3**(5), 493–513 (1993)
3. Y. Tanaka, Structural characterization of natural polyisoprenes: solve the mystery of natural rubber based on structural study. *Rubber Chem. Technol.* **74**(3), 355–375 (2001)
4. S. Toki et al., Entanglements and networks to strain-induced crystallization and stress-strain relations in natural rubber and synthetic polyisoprene at various temperatures. *Macromolecules* **46**(13), 5238–5248 (2013)
5. S. Toki et al., New insights into the relationship between network structure and strain-induced crystallization in un-vulcanized and vulcanized natural rubber by synchrotron X-ray diffraction. *Polymer* **50**(9), 2142–2148 (2009)
6. A.N. Gent, *Engineering with Rubber: How to Design Rubber Components* (Hanser Gardner, Cincinnati, 2001)
7. S. Trabelsi, P.A. Albouy, J. Rault, Stress-induced crystallization properties of natural and synthetic cis-polyisoprene. *Rubber Chem. Technol.* **77**(2), 303–316 (2004)
8. M. Tosaka et al., Crystallization of stretched network chains in cross-linked natural rubber. *J. Appl. Phys.* **101**, 084909 (2007)
9. Y. Miyamoto, H. Yamao, K. Sekimoto, Crystallization and melting of polyisoprene rubber under uniaxial deformation. *Macromolecules* **36**(17), 6462–6471 (2003)
10. M. Tosaka, Strain-induced crystallization of crosslinked natural rubber as revealed by X-ray diffraction using synchrotron radiation. *Polym. J.* **39**(12), 1207–1220 (2007)
11. G.G. Odian, *Principles of Polymerization* (Wiley, New York, 2007)
12. K. Nagdi, *Rubber as an Engineering Material: Guideline for Users* (Oxford University Press, New York, 1993)
13. G. Heideman et al., Activators in accelerated sulfur vulcanization. *Rubber Chem. Technol.* **77**(3), 512–541 (2004)
14. R. Steudel, Y. Steudel, Interaction of zinc oxide clusters with molecules related to the sulfur vulcanization of polyolefins (rubber). *Chem. Eur. J.* **12**(33), 8589–8602 (2006). ISSN: 1521-3765
15. P. Ghosh et al., Sulfur vulcanization of natural rubber for benzothiazole accelerated formulations: from reaction mechanisms to a rational kinetic model. *Rubber Chem. Technol.* **76**(3), 592–693 (2003). ISSN: 0035-9475
16. L.R.G. Treloar, *The Physics of Rubber Elasticity*, 3rd edn., Oxford Classic Texts in the Physical Sciences (Clarendon Press, Oxford, 2009)
17. J.S. Dick, *Rubber Technology: Compounding and Testing for Performance* (Hanser Gardner, Cincinnati, 2009). ISBN: 156990278X
18. B. Rodgers et al., *Carbon Black* (Marcel Dekker, New York, 2004)
19. M. Klüppel, A. Schröder, G. Heinrich, Carbon black, in *Physical Properties of Polymers Handbook*, ed. by M.E. James (Springer, New York, 2007). ISBN: 0387312358
20. M. Klüppel, G. Heinrich, Fractal structures in carbon black reinforced rubbers. *Rubber Chem. Technol.* **68**, 623 (1995)
21. G.J. Schneider et al., Correlation of mass fractal dimension and cluster size of silica in styrene butadiene rubber composites. *J. Chem. Phys.* **133**, 094902 (2010)
22. A.I. Medalia, F.A. Heckman, Morphology of aggregates II. Size and shape factors of carbon black aggregates from electron microscopy. *Carbon* **7**(5), 567–582 (1969)
23. T. Koga et al., New insight into hierarchical structures of carbon black dispersed in polymer matrices: a combined small-angle scattering study. *Macromolecules* **41**(2), 453–464 (2008)
24. J. Hyeon-Lee et al., Fractal analysis of flame-synthesized nanostructured silica and titania powders using small-angle X-ray scattering. *Langmuir* **14**(20), 5751–5756 (1998)

25. G.J. Schneider, D. Göritz, A novel model for the interpretation of small-angle scattering experiments of self-affine structures. *J. Appl. Crystallogr.* **43**(1), 12–16 (2009). ISSN: 0021-8898
26. D.J. Kohls, G. Beaucage, Rational design of reinforced rubber. *Curr. Opin. Solid State Mater. Sci.* **6**(3), 183–194 (2002). ISSN: 1359-0286
27. G.J. Schneider, Analyse der Struktur von aktiven Füllstoffen mittels Streumethoden. Ph.D. Thesis, Universität Regensburg (2006)
28. B.B. Mandelbrot, *The Fractal Geometry of Nature* (Times Books, New York, 1983)
29. M. Fleischmann, D.J. Tildesley, R.C. Ball, *Fractals in the Natural Sciences: A Discussion* (Princeton University Press, Princeton, 1990). ISBN: 0691085617
30. G. Huber, T.A. Vilgis, On the mechanism of hydrodynamic reinforcement in elastic composites. *Macromolecules* **35**(24), 9204–9210 (2002)
31. H.D. Bale, P.W. Schmidt, Small-angle X-ray-scattering investigation of submicroscopic porosity with fractal properties. *Phys. Rev. Lett.* **53**(6), 596–599 (1984)
32. P.W. Schmidt, Small-angle scattering studies of disordered, porous and fractal systems. *J. Appl. Crystallogr.* **24**(5), 414–435 (1991)
33. N. Stribeck, *X-Ray Scattering of Soft Matter* (Springer, Heidelberg, 2007)
34. J.E. Martin, Scattering exponents for polydisperse surface and mass fractals. *J. Appl. Crystallogr.* **19**(1), 25–27 (1986). ISSN: 0021-8898
35. G. Beaucage et al., Morphology of polyethylene-carbon black composites. *J. Polym. Sci. B Polym. Phys.* **37**(11), 1105–1119 (1999). ISSN: 1099-0488
36. R. Hjelm et al., The microstructure and morphology of carbon black: a study using small angle neutron scattering and contrast variation. *J. Mater. Res.* **9**(12), 3210–3222 (1994)
37. W. Ruland, Apparent fractal dimensions obtained from small-angle scattering of carbon materials. *Carbon* **39**(2), 323–324 (2001)
38. G. Heinrich, M. Klüppel, A hypothetical mechanism of carbon black formation based on molecular ballistic deposition. *Kautschuk, Gummi, Kunststoffe* **54**(4), 159–165 (2001)
39. G. Beaucage, Approximations leading to a unified exponential/power-law approach to small-angle scattering. *J. Appl. Crystallogr.* **28**(6), 717–728 (1995)
40. M. Klüppel, The role of disorder in filler reinforcement of elastomers on various length scales. *Adv. Polym. Sci.* **164**, 1–86 (2003)
41. A. Schröder, M. Klüppel, R. Schuster, Characterisation of surface activity of carbon black and its relation to polymer-filler interaction. *Macromol. Mater. Eng.* **292**(8), 885–916 (2007)
42. T.P. Rieker, S. Misono, F. Ehrburger-Dolle, Small-angle X-ray scattering from carbon blacks: crossover between the fractal and Porod regimes. *Langmuir* **15**(4), 914–917 (1999)
43. T.P. Rieker, M. Hindermann-Bischoff, F. Ehrburger-Dolle, Small-angle X-ray scattering study of the morphology of carbon black mass fractal aggregates in polymeric composites. *Langmuir* **16**(13), 5588–5592 (2000)
44. J. Fröhlich, S. Kreitmeier, D. Göritz, Surface characterization of carbon blacks. *Kautsch. Gummi Kunstst.* **51**, 370–376 (1998)
45. C.R. Herd, G.C. McDonald, W.M. Hess, Morphology of carbon-black aggregates: fractal versus Euclidean geometry. *Rubber Chem. Technol.* **65**, 107 (1992)
46. R. Botet, R. Jullien, Fractal aggregates of particles. *Phase Trans. Multinat. J.* **24**(2), 691–736 (1990)
47. T.C. Gruber, T.W. Zerda, M. Gerspacher, 3D morphological characterization of carbon-black aggregates using transmission electron microscopy. *Rubber Chem. Technol.* **67**(2), 280–287 (1994)
48. J. Feder, *Fractals* (Plenum Press, New York, 1988)
49. K.J. Falconer, *Fractal Geometry* (Wiley, New York, 1990)
50. G. Heinrich, M. Klüppel, T. Vilgis, Reinforcement theories, in *Physical Properties Of Polymers Handbook*, ed. by M.E. James (Springer, New York, 2007). ISBN: 0387312358
51. D.C. Edwards, Polymer-filler interactions in rubber reinforcement. *J. Mater. Sci.* **25**(10), 4175–4185 (1990)

52. T.A. Vilgis, G. Heinrich, Disorder-induced enhancement of polymer adsorption—a model for the rubber-polymer interaction in filled rubbers. *Macromolecules* **27**(26), 7846–7854 (1994)
53. A.R. Payne, Dynamic properties of heat-treated butyl vulcanizates. *J. Appl. Polym. Sci.* **7**, 873–885 (1963)
54. S. Merabia, P. Sotta, D.R. Long, A microscopic model for the reinforcement and the nonlinear behavior of filled elastomers and thermoplastic elastomers (Payne and Mullins effects). *Macromolecules* **41**(21), 8252–8266 (2008)
55. S.D. Gehman, J.E. Field, X-ray structure of rubber-carbon black mixtures. *Ind. Eng. Chem.* **32**(10), 1401–1407 (1940)
56. J. Domurath et al., Modelling of stress and strain amplification effects in filled polymer melts. *J. Non-Newton. Fluid Mech.* **171**, 8–16 (2012)
57. L. Mullins, N.R. Tobin, Stress softening in rubber vulcanizates. I. Use of a strain-amplification factor to describe the elastic behavior of filler-reinforced vulcanized rubber. *J. Appl. Polym. Sci.* **9**, 2993 (1965)
58. A.I. Medalia, Morphology of aggregates: I. Calculation of shape and bulkiness factors; application to computer-simulated random flows. *J. Colloid Interface Sci.* **24**(3), 393–404 (1967)
59. S. Westermann et al., Strain amplification effects in polymer networks. *Physica B: Cond. Matter* **234**, 306–307 (1997). ISSN: 0921-4526
60. J. Rault et al., Stress-induced crystallization and reinforcement in filled natural rubbers: 2H NMR study. *Macromolecules* **39**(24), 8356–8368 (2006)
61. G. Huber, T.A. Vilgis, Universal properties of filled rubbers: mechanisms for reinforcement on different length scales. *Kautsch. Gummi Kunstst.* **52**(2), 102–107 (1999)
62. D.J. Lee, J.A. Donovan, Microstructural changes in the crack tip region of carbon-black-filled natural rubber. *Rubber Chem. Technol.* **60**(5), 910–923 (1987)
63. J.A.C. Harwood, L. Mullins, A.R. Payne, Stress softening in natural rubber vulcanizates. Part II. Stress softening effects in pure gum and filler loaded rubbers. *J. Appl. Polym. Sci.* **9**(9), 3011–3021 (1965)
64. S. Dupres et al., Local deformation in carbon black-filled polyisoprene rubbers studied by NMR and X-ray diffraction. *Macromolecules* **42**(7), 2634–2644 (2009)
65. S. Westermann et al., Matrix chain deformation in reinforced networks: a SANS approach. *Macromolecules* **32**(18), 5793–5802 (1999). ISSN: 0024-9297
66. A. Botti et al., A microscopic look at the reinforcement of silica-filled rubbers. *J. Chem. Phys.* **124**, 174908 (2006)
67. N. Jouault et al., Direct small-angle-neutron-scattering observation of stretched chain conformation in nanocomposites: more insight on polymer contributions in mechanical reinforcement. *Phys. Rev. E* **82**(3), 31801 (2010). ISSN: 1063-651X
68. S. Trabelsi, P.A. Albouy, J. Rault, Effective local deformation in stretched filled rubber. *Macromolecules* **36**(24), 9093–9099 (2003)
69. K. Brüning, K. Schneider, G. Heinrich, Deformation and orientation in filled rubbers on the nano- and microscale studied by X-ray scattering. *J. Polym. Sci. B Polym. Phys.* **50**(24), 1728–1732 (2012)
70. T. Witten, M. Rubinstein, R. Colby, Reinforcement of rubber by fractal aggregates. *J. Phys. II* **3**(3), 367–383 (1993)
71. J. Fröhlich, W. Niedermeier, H.-D. Luginsland, The effect of filler-filler and filler-elastomer interaction on rubber reinforcement. *Compos. A Appl. Sci. Manuf.* **36**(4), 449–460 2005. ISSN: 1359-835X. doi:10.1016/j.compositesa.2004.10.004, <http://www.sciencedirect.com/science/article/B6TWN-4F0854M-5/2/e872fc26f9297bbc0c83c9e362647db3>
72. T. Lanzl, Charakterisierung von Ruß-Kautschuk-Mischungen mittels dielektrischer Spektroskopie. Ph.D. Thesis, Universität Regensburg (2001)
73. V.M. Litvinov, P.A.M. Steeman, EPDM-carbon black interactions and the reinforcement mechanisms, as studied by low-resolution ¹H NMR. *Macromolecules* **32**(25), 8476–8490 (1999)
74. S. Wolff, M.J. Wang, E.H. Tan, Filler-elastomer interactions. Part VII. Study on bound rubber. *Rubber Chem. Technol.* **66**(2), 163–177 (1993)

75. S. Kohjiya, A. Kato, Y. Ikeda, Visualization of nanostructure of soft matter by 3D-TEM: nanoparticles in a natural rubber matrix. *Progr. Polym. Sci.* **33**(10), 979–997 (2008)
76. S. Kohjiya et al., Visualisation of carbon black networks in rubbery matrix by skeletonisation of 3D-TEM image. *Polymer* **47**(10), 3298–3301 (2006)
77. M.-J. Wang, Effect of polymer-filler and filler-filler interactions on dynamic properties of filled vulcanizates. *Rubber Chem. Technol.* **71**(3), 520–589 (1998)
78. J.T. Bauman, *Fatigue, Stress, and Strain of Rubber Components: Guide for Design Engineers* (Hanser, Cincinnati, 2008)
79. S. Toki et al., Multi-scaled microstructures in natural rubber characterized by synchrotron X-ray scattering and optical microscopy. *J. Polym. Sci. A Polym. Chem.* **46**(22), 2456–2464 (2008)
80. W.R. Krigbaum et al., Effect of strain on the thermodynamic melting temperature of polymers. *J. Polym. Sci. A-2 Polym. Phys.* **4**(3), 475–489 (1966)
81. W.R. Krigbaum, R.J. Roe, Diffraction study of crystallite orientation in a stretched polychloroprene vulcanizate. *J. Polym. Sci. A General Papers* **2**(10), 4391–4414 (1964)
82. M. Tsuji, T. Shimizu, S. Kohjiya, TEM studies on thin films of natural rubber and polychloroprene crystallized under molecular orientation II. Highly prestretched thin films. *Polym. J.* **32**(6), 505–512 (2000)
83. M. Tsuji, T. Shimizu, S. Kohjiya, TEM studies on thin films of natural rubber and polychloroprene crystallized under molecular orientation. *Polym. J.* **31**(9), 784–789 (1999)
84. S. Toki et al., Structural developments in synthetic rubbers during uniaxial deformation by in situ synchrotron X-ray diffraction. *J. Polym. Sci. B Polym. Phys.* **42**(6), 956–964 (2004)
85. S. Toki et al., Strain-induced molecular orientation and crystallization in natural and synthetic rubbers under uniaxial deformation by in-situ synchrotron X-ray study. *Rubber Chem. Technol.* **77**, 317 (2004)
86. G.R. Mitchell, A wide-angle X-ray study of the development of molecular orientation in crosslinked natural rubber. *Polymer* **25**(11), 1562–1572 (1984)
87. M. Kroon, A constitutive model for strain-crystallising rubber-like materials. *Mech. Mater.* **42**(9), 873–885 (2010). ISSN: 0167-6636. doi:10.1016/j.mechmat.2010.07.008, <http://www.sciencedirect.com/science/article/pii/S0167663610000980>
88. W.V. Mars, A. Fatemi, A phenomenological model for the effect of R ratio on fatigue of strain crystallizing rubbers. *Rubber Chem. Technol.* **76**(5), 1241–1258 (2003)
89. R.S. Stein, J. Powers, *Topics in Polymer Physics* (Imperial College Press, Singapore, 2006)
90. L.H. Sperling, *Introduction to Physical Polymer Science* (Wiley, New York, 1992)
91. G. Marckmann, E. Verron, Comparison of hyperelastic models for rubber-like materials. *Rubber Chem. Technol.* **79**(5), 835–858 (2006)
92. L. Mullins, N.R. Tobin, Theoretical model for the elastic behavior of filler-reinforced vulcanized rubbers. *Rubber Chem. Technol.* **30**(2), 555–571 (1957)
93. F. Bueche, Mullins effect and rubber-filler interaction. *J. Appl. Polym. Sci.* **5**(15), 271–281 (1961)
94. G. Heinrich, M. Klüppel, Recent advances in the theory of filler networking in elastomers. *Adv. Polym. Sci.* **160**(1), 1–44 (2002)
95. S. Richter et al., Jamming in filled polymer systems. *Macromol. Symp.* **291**(1), 193–201 (2010). ISSN: 1521-3900
96. S.M. Cadwell et al., Dynamic fatigue life of rubber. *Ind. Eng. Chem. Anal. Ed.* **12**(1), 19–23 (1940)
97. W.V. Mars, A. Fatemi, A literature survey on fatigue analysis approaches for rubber. *Int. J. Fatigue* **24**(9), 949–961 (2002)
98. A. Andriyana, N. Saintier, E. Verron, Multiaxial fatigue life prediction of rubber using configurational mechanics and critical plane approaches: a comparative study, in *Proceedings of the VI. European Conference on Constitutive Models for Rubber*, vol. 5, ed. by P.E. Austrell, L. Kari (Balkema, Tokyo, 2008), p. 191
99. W.V. Mars, A. Fatemi, Factors that affect the fatigue life of rubber: a literature survey. *Rubber Chem. Technol.* **77**, 391–412 (2004)

100. W.V. Mars, A. Fatemi, Nucleation and growth of small fatigue cracks in filled natural rubber under multiaxial loading. *J. Mater. Sci.* **41**(22), 7324–7332 (2006)
101. J.B. Le Cam et al., Mechanism of fatigue crack growth in carbon black filled natural rubber. *Macromolecules* **37**(13), 5011–5017 (2004)
102. A.G. Thomas, The development of fracture mechanics for elastomers. *Rubber Chem. Technol.* **67**(3), 50–67 (1994)
103. R.S. Rivlin, A.G. Thomas, Rupture of rubber. I. Characteristic energy for tearing. *J. Polym. Sci.* **10**(3), 291–318 (1953)
104. W.V. Mars, A. Fatemi, Fatigue crack nucleation and growth in filled natural rubber. *Fatigue Fract. Eng. Mater. Struct.* **26**(9), 779–789 (2003)
105. A.G. Thomas, Rupture of rubber. II. The strain concentration at an incision. *J. Polym. Sci.* **18**(88), 177–188 (1955)
106. G. Andreini et al., Crack growth behavior of styrene-butadiene rubber, natural rubber, and polybutadiene rubber compounds: comparison of pure-shear versus strip tensile test. *Rubber Chem. Technol.* **86**(1), 132–145 (2013)
107. J.B. Le Cam, E. Toussaint, The mechanism of fatigue crack growth in rubbers under severe loading: the effect of stress-induced crystallization. *Macromolecules* **43**(10), 4708–4714 (2010)
108. J.R. Rice, A path independent integral and the approximate analysis of strain concentration by notches and cracks. *J. Appl. Mech.* **35**, 379–386 (1968)
109. G. Cherepanov, Crack propagation in continuous media. *J. Appl. Math. Mech.* **31**, 503–512 (1967)
110. N. Ait Hocine, M. Nait Abdelaziz, Fracture analysis of rubber-like materials using global and local approaches: initiation and propagation direction of a crack. *Polym. Eng. Sci.* **49**(6), 1076–1088 (2009)
111. T. Horst, Spezifische Ansätze zur bruchmechanischen Charakterisierung von Elastomeren. Ph.D. Thesis, Universität Dresden (2010)
112. K.H. Schwalbe, Approximate calculation of fatigue crack growth. *Int. J. Fract.* **9**(4), 381–395 (1973)
113. G. Andreini et al., Comparison of sine versus pulse waveform effects on fatigue crack growth behavior of NR, SBR, and BR compounds. *Rubber Chem. Technol.* **83**(4), 391–403 (2010)
114. U.G. Eisele, S.A. Kelbch, A.J.M. Summer, Crack growth performance of tire compounds. *Rubber World* **212**, 38–45 (1995)
115. R.J. Harbour, A. Fatemi, W.V. Mars, The effect of a dwell period on fatigue crack growth rates in filled SBR and NR. *Rubber Chem. Technol.* **80**(5), 838–853 (2007)
116. E.H. Andrews, Crack propagation in a strain-crystallizing elastomer. *J. Appl. Phys.* **32**(3), 542–548 (1961)
117. R.J. Harbour, A. Fatemi, W.V. Mars, Fatigue crack growth of filled rubber under constant and variable amplitude loading conditions. *Fatigue Fract. Eng. Mater. Struct.* **30**(7), 640–652 (2007)
118. A.T. Zehnder, *Fracture Mechanics* (Springer, New York, 2012)
119. N. Saintier, G. Cailletaud, R. Piques, Cyclic loadings and crystallization of natural rubber: an explanation of fatigue crack propagation reinforcement under a positive loading ratio. *Mater. Sci. Eng. A* **528**(3), 1078–1086 (2011). ISSN: 0921-5093. doi:[10.1016/j.msea.2010.09.079](https://doi.org/10.1016/j.msea.2010.09.079), <http://www.sciencedirect.com/science/article/pii/S0921509310011251>
120. W.F. Busse, Tear resistance and structure of rubber. *Ind. Eng. Chem.* **26**(11), 1194–1199 (1934)
121. W.V. Mars, Computed dependence of rubber's fatigue behavior on strain crystallization. *Rubber Chem. Technol.* **82**, 51–61 (2009)
122. N. Andre, G. Cailletaud, R. Piques, Haigh diagram for fatigue crack initiation prediction of natural rubber components. *Kautsch. Gummi Kunstst.* **52**(2), 120–123 (1999)
123. H.W. Greensmith, Rupture of rubber. IV. Tear properties of vulcanizates containing carbon black. *J. Polym. Sci.* **21**(98), 175–187 (1956)

124. K. Sakulkaew, A.G. Thomas, J.J.C. Busfield, The effect of the rate of strain on tearing in rubber. *Polym. Testing* **30**(2), 163–172 (2011)
125. B. Gabrielle et al., Tear rotation in reinforced natural rubber, in *Proceedings of the VII. European Conference on Constitutive Models for Rubber* (2011), pp. 221–225
126. B. Gabrielle et al., Effect of tear rotation on ultimate strength in reinforced natural rubber. *Macromolecules* **44**(17), 7006–7015 (2011)
127. J.B. Brunac, O. Gérardin, J.B. Leblond, On the heuristic extension of Haigh's diagram for the fatigue of elastomers to arbitrary loadings. *Int. J. Fatigue* **31**(5), 859–867 (2009)
128. W.V. Mars, A. Fatemi, Multiaxial fatigue of rubber: Part I: Equivalence criteria and theoretical aspects. *Fatigue Fract. Eng. Mater. Struct.* **28**(6), 515–522 (2005)
129. W.V. Mars, A. Fatemi, Multiaxial stress effects on fatigue behavior of filled natural rubber. *Int. J. Fatigue* **28**(5-6), 521–529 (2006)
130. S.V. Hainsworth, An environmental scanning electron microscopy investigation of fatigue crack initiation and propagation in elastomers. *Polym. Testing* **26**(1), 60–70 (2007)
131. D.K. Setua, S.K. De, Scanning electron microscopy studies on mechanism of tear fracture of styrene-butadiene rubber. *J. Mater. Sci.* **18**(3), 847–852 (1983)
132. K. Legorju-Jago, C. Bathias, Fatigue initiation and propagation in natural and synthetic rubbers. *Int. J. Fatigue* **24**(2-4), 85–92 (2002)
133. D.G. Young, Dynamic property and fatigue crack propagation research on tire sidewall and model compounds. *Rubber Chem. Technol.* **58**(4), 785–805 (1985)
134. DESY website, http://photon-science.desy.de/facilities/petra_iii/index_eng.html. Accessed 16 May 2013
135. Lecture Notes "Physik mit Synchrotronstrahlung", given by Prof. C. Schroer, TU Dresden (2011)
136. A. Guinier et al., *Small-Angle Scattering of X-Rays* (Wiley, New York, 1955)
137. L.A. Feigin, D.I. Svergun, *Structure Analysis by Small-Angle X-Ray and Neutron Scattering* (Plenum Press, New York, 1987)
138. O. Glatter, O. Kratky, *Small Angle X-Ray Scattering* (Academic Press, London, 1982)
139. P. Lindner, T. Zemb, *Neutrons, X-Rays, and Light: Scattering Methods Applied to Soft Condensed Matter* (Elsevier North-Holland, Boston, 2002)
140. B.J. Berne, R. Pecora, *Dynamic Light Scattering, with Applications to Chemistry, Biology, and Physics* (Dover, New York, 2000)
141. C.G. Vonk, G. Kortleve, X-ray small-angle scattering of bulk polyethylene. *Colloid Polym. Sci.* **220**(1), 19–24 (1967)
142. G. Beaucage, H.K. Kammler, S.E. Pratsinis, Particle size distributions from small-angle scattering using global scattering functions. *J. Appl. Crystallogr.* **37**(4), 523–535 (2004)
143. J. Fröhlich, Analyse der räumlichen Struktur und der Oberfläche von aktiven Füllstoffen mittels Streumethoden. Ph.D. Thesis, Universität Regensburg (1998)
144. H. Zhang et al., Nanocavitation in carbon black filled styrene-butadiene rubber under tension detected by real time small angle X-ray scattering. *Macromolecules* **45**(3), 1529–1543 (2012)
145. A. Jánosi, Röntgenkleinwinkelstreuung von Mehrphasensystemen, interpretation der Elektromagnetischen Fluktuation: II. Dreiphasensysteme. *Monatsh. Chem. Chem. Mon.* **114**(4), 383–387 (1983)
146. P.P. Ewald, Introduction to the dynamical theory of X-ray diffraction. *Acta Crystallogr. A Cryst. Phys. Diff. Theor. General Crystallogr.* **25**(1), 103–108 (1969)
147. W.H. Bragg, W.L. Bragg, The reflection of X-rays by crystals. *Proc. R. Soc. Lond. Ser. A* **88**(605), 428–438 (1913)
148. L.E. Alexander, *X-Ray Diffraction Methods in Polymer Science* (Wiley-Interscience, New York, 1969)
149. G.K. Elyashevich, Thermodynamic and kinetics of orientational crystallization of flexible-chain polymers. *Adv. Polym. Sci.* **43**, 205–245 (1982). ISSN: 0065-3195
150. S. Rabiej, A comparison of two X-ray diffraction procedures for crystallinity determination. *Eur. Polym. J.* **27**(9), 947–954 (1991)

151. M. Tosaka et al., Orientation and crystallization of natural rubber network as revealed by WAXD using synchrotron radiation. *Macromolecules* **37**(9), 3299–3309 (2004)
152. J.M. Goppel, On the degree of crystallinity in natural rubber. *Appl. Sci. Res.* **1**(1), 3–17 (1949)
153. S.C. Nyburg, X-ray determination of crystallinity in deformed natural rubber. *Br. J. Appl. Phys.* **5**, 321–324 (1954)
154. R. Oono, K. Miyasaka, K. Ishikawa, Crystallization kinetics of biaxially stretched natural rubber. *J. Polym. Sci. Polym. Phys. Ed.* **11**(8), 1477–1488 (1973)
155. P. Bansal et al., Multivariate statistical analysis of X-ray data from cellulose: a new method to determine degree of crystallinity and predict hydrolysis rates. *Bioresour. Technol.* **101**(12), 4461–4471 (2010)
156. J.R. Katz, Röntgenspektrographische Untersuchungen am gedehnten Kautschuk und ihre mögliche Bedeutung für das Problem der Dehnungseigenschaften dieser Substanz. *Naturwissenschaften* **13**(19), 410–416 (1925)
157. C.W. Bunn, Molecular structure and rubber-like elasticity. I. The crystal structures of gutta-percha, rubber and polychloroprene. *Proc. R. Soc. Lond. Ser. A. Math. Phys. Sci.* **180**(980), 40 (1942)
158. A. Immirzi et al., Crystal structure and melting entropy of natural rubber. *Macromolecules* **38**(4), 1223–1231 (2005)
159. Y. Takahashi, T. Kumano, Crystal structure of natural rubber. *Macromolecules* **37**(13), 4860–4864 (2004)
160. S.C. Nyburg, A statistical structure for crystalline rubber. *Acta Crystallogr. A* **7**(5), 385–392 (1954)
161. G. Natta, P. Corradini, über die Kristallstrukturen des 1,4-cis-polybutadiens und des 1,4-cis-polyisoprens. *Angew. Chem.* **68**(19), 615–616 (1956)
162. W. Yau, R.S. Stein, Optical studies of the stress-induced crystallization of rubber. *J. Polym. Sci. A-2 Polym. Phys.* **6**(1), 1–30 (1968)
163. L.A. Wood, N. Bekkedahl, Crystallization of unvulcanized rubber at different temperatures. *J. Appl. Phys.* **17**, 362 (1946)
164. E.N. Dalal, K.D. Taylor, P.J. Phillips, The equilibrium melting temperature of cis-polyisoprene. *Polymer* **24**(12), 1623–1630 (1983)
165. B. Huneau, Strain-induced crystallization of natural rubber: a review of X-ray diffraction investigations. *Rubber Chem. Technol.* **84**(3), 425–452 (2011). doi:[10.5254/1.3601131](https://doi.org/10.5254/1.3601131). <http://link.aip.org/link/RCT/84/425/1>
166. E.H. Andrews, Spherulite morphology in thin films of natural rubber. *Proc. R. Soc. Lond. Ser. A Math. Phys. Sci.* **270**(1341), 232–241 (1962)
167. E.H. Andrews, Crystalline morphology in thin films of natural rubber. II. Crystallization under strain. *Proc. R. Soc. Lond. Ser. A Math. Phys. Sci.* **277**(1371), 562–570 (1964)
168. S. Kawahara et al., Crystal nucleation and growth of natural rubber purified by deproteinization and trans-esterification. *Polym. J.* **36**(5), 361–367 (2004)
169. D. Luch, G.S.Y. Yeh, Morphology of strain-induced crystallization of natural rubber. Part II. X-ray studies on cross-linked vulcanizates. *J. Macromol. Sci. B* **7**(1), 121–155 (1973)
170. L. Mandelkern, *Crystallization of Polymers Volume 1: Equilibrium Concepts* (Cambridge University Press, Cambridge, 2004)
171. E.H. Andrews, P.J. Owen, A. Singh, Microkinetics of lamellar crystallization in a long chain polymer. *Proc. R. Soc. Lond. Ser. A Math. Phys. Sci.* **324**(1556), 79–97 (1971)
172. G.S.Y. Yeh, Strain-induced crystallization II. Subsequent fibrillar-to-lamellar transformation. *Polym. Eng. Sci.* **16**(3), 145–151 (1976)
173. G.S.Y. Yeh, Morphology of strain-induced crystallization of polymers. Part I. Rubber Chem. Technol. **50**, 863–873 (1977)
174. T. Shimizu et al., TEM observation of natural rubber thin films crystallized under molecular orientation. *Rubber Chem. Technol.* **73**(5), 926–936 (2000)
175. J.H. Magill, Crystallization and morphology of rubber. *Rubber Chem. Technol.* **68**, 507–539 (1995)

176. W.F. Reichert, M.K. Hopfenmüller, D. Göritz, Volume change and gas transport at uniaxial deformation of filled natural rubber. *J. Mater. Sci.* **22**(10), 3470–3476 (1987)
177. S.R. Ryu, J.W. Sung, D.J. Lee, Strain-induced crystallization and mechanical properties of NBR composites with carbon nanotube and carbon black. *Rubber Chem. Technol.* **85**(2), 207–218 (2012)
178. S. Trabelsi, P.A. Albouy, J. Rault, Crystallization and melting processes in vulcanized stretched natural rubber. *Macromolecules* **36**(20), 7624–7639 (2003)
179. M.F. Acken, W.E. Singer, W. Davey, X-ray study of rubber structure. *Ind. Eng. Chem.* **24**(1), 54–57 (1932)
180. H. Hiratsuka et al., Measurement of orientation crystallization rates of linear polymers by means of dynamic X-ray diffraction technique. II. Frequency dispersion of strain-induced crystallization coefficient of natural rubber vulcanizates in subsonic range. *J. Macromol. Sci. B* **8**(1–2), 101–126 (1973). doi:[10.1080/00222347308245796](https://doi.org/10.1080/00222347308245796), eprint: <http://www.tandfonline.com/doi/pdf/10.1080/00222347308245796>, <http://www.tandfonline.com/doi/abs/10.1080/00222347308245796>
181. H. Kawai, Dynamic X-ray diffraction technique for measuring rheo-optical properties of crystalline polymeric materials. *Rheol. Acta* **14**(1), 27–47 (1975). ISSN: 0035-4511, <http://dx.doi.org/10.1007/BF01527209>
182. N. Candau et al., Characteristic time of strain induced crystallization of crosslinked natural rubber. *Polymer* **53**(13), 2540–2543 (2012)
183. I. Temizer, P. Wriggers, T.J.R. Hughes, Contact treatment in isogeometric analysis with NURBS. *Comput. Methods Appl. Mech. Eng.* **200**(9), 1100–1112 (2011)
184. D.J. Dunning, P.J. Pennells, Effect of strain on rate of crystallization of natural rubber. *Rubber Chem. Technol.* **40**, 1381 (1967)
185. J.C. Mitchell, D.J. Meier, Rapid stress-induced crystallization in natural rubber. *J. Polym. Sci. A-2 Polym. Phys.* **6**(10), 1689–1703 (1968)
186. M. Tosaka et al., Crystallization and stress relaxation in highly stretched samples of natural rubber and its synthetic analogue. *Macromolecules* **39**(15), 5100–5105 (2006)
187. M. Tosaka et al., Detection of fast and slow crystallization processes in instantaneously-strained samples of cis-1,4-polyisoprene. *Polymer* **53**(3), 864–872 (2012)
188. L. Mandelkern, *Crystallization of Polymers Volume 2: Kinetics and Mechanisms* (Cambridge University Press, Cambridge, 2004)
189. P.G. De Gennes, Coil-stretch transition of dilute flexible polymers under ultrahigh velocity gradients. *J. Chem. Phys.* **60**(12), 5030–5042 (1974)
190. R.H. Somani et al., Flow-induced shish-kebab precursor structures in entangled polymer melts. *Polymer* **46**(20), 8587–8623 (2005)
191. J.F. Sanders, J.D. Ferry, R.H. Valentine, Viscoelastic properties of 1,2- polybutadiene: comparison with natural rubber and other elastomers. *J. Polym. Sci. A-2 Polym. Phys.* **6**(5), 967–980 (1968)
192. M. Rubinstein, R.H. Colby, *Polymer Physics* (Oxford University Press, Oxford, 2003)
193. L. Mandelkern, Crystallization kinetics of homopolymers: overall crystallization: a review. *Biophys. Chem.* **112**(2–3), 109–116 (2004)
194. C. Fond, Cavitation criterion for rubber materials: a review of void-growth models. *J. Polym. Sci. B Polym. Phys.* **39**(17), 2081–2096 (2001)
195. A. Dorfmann, K.N.G. Fuller, R.W. Ogden, Shear, compressive and dilatational response of rubberlike solids subject to cavitation damage. *Int. J. Solids Struct.* **39**(7), 1845–1861 (2002)
196. A.N. Gent, P.B. Lindley, Tension flaws in bonded cylinders of soft rubber. *Rubber Chem. Technol.* **31**(2), 393–394 (1958)
197. P. Adriaensens et al., Relationships between microvoid heterogeneity and physical properties in cross-linked elastomers: an NMR imaging study. *Macromolecules* **33**(19), 7116–7121 (2000)
198. J.B. Le Cam, A review of volume changes in rubbers: the effect of stretching. *Rubber Chem. Technol.* **83**, 247 (2010)

199. A.N. Gent, Cavitation in rubber: a cautionary tale. *Rubber Chem. Technol.* **63**(3), 49–53 (1990)
200. R. Christensen, C. Hoeve, Theoretical and experimental values of the volume changes accompanying rubber extension. *Rubber Chem. Technol.* **43**, 1473–1481 (1970)
201. R.W. Penn, Volume changes accompanying the extension of rubber. *J. Rheol.* **14**, 509–517 (1970)
202. T. Shinomura, M. Takahashi, Volume change measurements of filled rubber vulcanizates under stretching. *Rubber Chem. Technol.* **43**, 1025–1035 (1970)
203. R. Shuttleworth, Volume change measurements in the study of rubber-filler interactions. *Eur. Polym. J.* **4**(1), 31–38 (1968)
204. S. Kaneko, J.E. Frederick, D. McIntyre, Void formation in a filled SBR rubber determined by small-angle X-ray scattering. *J. Appl. Polym. Sci.* **26**(12), 4175–4192 (1981)
205. J. Ramier et al., In situ SALS and volume variation measurements during deformation of treated silica filled SBR. *J. Mater. Sci.* **42**(19), 8130–8138 (2007)
206. K. Layouni, L. Laiarinandrasana, R. Piques, Compressibility induced by damage in carbon black reinforced natural rubber, in *Proceedings of the III. European Conference on Constitutive Models for Rubber*, ed. by J.C.C. Busfield, A.H. Muhr (Taylor & Francis, London, 2003), p. 273
207. J.B. Le Cam, E. Toussaint, Cyclic volume changes in rubber. *Mech. Mater.* **41**(7), 898–901 (2009)
208. J.B. Le Cam, E. Toussaint, Volume variation in stretched natural rubber: competition between cavitation and stress-induced crystallization. *Macromolecules* **41**(20), 7579–7583 (2008)
209. T. Shinomura, M. Takahashi, Morphological study on carbon black loaded rubber vulcanizate under stretching. *Rubber Chem. Technol.* **43**, 1015–1024 (1970)
210. E. Bayraktar et al., Damage mechanisms in natural (NR) and synthetic rubber (SBR): nucleation, growth and instability of the cavitation. *Fatigue Fract. Eng. Mater. Struct.* **31**(2), 184–196 (2008)
211. P.A. Kakavas, W.V. Chang, Acoustic emission in bonded elastomer discs subjected to compression. *J. Appl. Polym. Sci.* **45**(5), 865–869 (1992)
212. J.C. Goebel, A.V. Tobolsky, Volume change accompanying rubber extension. *Macromolecules* **4**(2), 208–209 (1971)
213. J.M. Chenal et al., Parameters governing strain induced crystallization in filled natural rubber. *Polymer* **48**(23), 6893–6901 (2007)
214. A.N. Gent, B. Park, Failure processes in elastomers at or near a rigid spherical inclusion. *J. Mater. Sci.* **19**(6), 1947–1956 (1984)
215. A.N. Gent, P.B. Lindley, Internal rupture of bonded rubber cylinders in tension. *Proc. R. Soc. Lond. Ser. A Math. Phys. Sci.* **249**(1257), 195–205 (1959)
216. K. Cho, A.N. Gent, Cavitation in model elastomeric composites. *J. Mater. Sci.* **23**(1), 141–144 (1988)
217. A.N. Gent, D.A. Tompkins, Nucleation and growth of gas bubbles in elastomers. *J. Appl. Phys.* **40**, 2520 (1969)
218. P. Kumar et al., Volume changes under strain resulting from the incorporation of rubber granulates into a rubber matrix. *J. Polym. Sci. B Polym. Phys.* **45**(23), 3169–3180 (2007)

In-situ Structure Characterization of Elastomers during
Deformation and Fracture

Brüning, K.

2014, XIV, 124 p. 82 illus., 51 illus. in color., Hardcover

ISBN: 978-3-319-06906-7